UNIVERSITÀ DEGLI STUDI DI PAVIA

FACULTY OF ENGINEERING

DEPARTMENT OF ELECTRICAL, COMPUTER AND BIOMEDICAL ENGINEERING

MASTER'S DEGREE IN ELECTRONIC ENGINEERING

MASTER'S DEGREE THESIS

Sviluppo e progettazione di un sensore a microonde basato sull'analisi della variazione di fase

---

Implementation and Design of a Microwave Sensor Leveraging the Phase Variation Analysis

---

Supervisors: Prof. Maurizio Bozzi
Prof. Michal Mrozowski

Candidate: Ehsan Zehtabchi
Student ID: 501728

September - 2025

Dedicated to my family.

طی شد ایام برومندی ما در سختی
همچو آن دانه که در زیر قدم سبز شود.
صائب تبریزی (11 هجری)

The days of our dignity passed in hardship,
Like that seed which turns green beneath the foot.
Saib Tabrizi, 17th Century AD

UNIVERSITÀ DEGLI STUDI DI PAVIA

Abstract

Sommario-Italiano

Questa tesi presenta la progettazione, l'implementazione e l'analisi di un sensore a microonde basato sulla variazione di fase per la misurazione degli spostamenti. Il sensore sfrutta i principi dell'interferometria e dei risonatori a anello aperto (Split-Ring Resonators, SRR) per ottenere un'elevata sensibilità e accuratezza nel rilevamento di spostamenti senza contatto. Lo studio esplora varie configurazioni, inclusi setup interferometrici complementari di tipo Michelson e Mach-Zehnder, per convertire le variazioni di fase in variazioni di ampiezza misurabili, semplificando così il processo di rilevamento.

Questa ricerca inizia con una revisione approfondita dei sensori a microonde esistenti e delle loro applicazioni nel rilevamento di umidità, caratterizzazione dei materiali, rilevamento di crepe e misurazione degli spostamenti. Si procede quindi a stabilire le basi teoriche delle linee microstrip, degli accoppiatori direzionali e degli SRR, prima di progettare e simulare un accoppiatore ibrido a branch-line (Branch-Line Hybrid Coupler, BLHC) ottimizzato per l'analisi di fase. I risultati confermano una risposta di fase lineare con una sensibilità di 12°/mm, dimostrando la precisione del sensore nel rilevamento di spostamenti. Per convalidare le prestazioni, sono state condotte simulazioni elettromagnetiche a onda intera (full-wave) utilizzando ADS, CST e HFSS, che hanno mostrato una sensibilità allo spostamento fino a 3.6 dB/mm.

La convalida sperimentale è stata condotta utilizzando prototipi realizzati, con misurazioni che si allineano strettamente ai risultati delle simulazioni. Il sensore proposto presenta vantaggi quali dimensioni compatte e robustezza. Le potenziali applicazioni includono il monitoraggio dell'integrità strutturale, sensori biomedicali e automazione industriale. I futuri sviluppi potranno concentrarsi sulla miniaturizzazione, sul rilevamento multi-parametro e sull'integrazione con sistemi wireless per il monitoraggio in tempo reale.

Abstract - English

This thesis presents the design, implementation, and analysis of a microwave sensor based on phase variation for displacement measurement. The sensor leverages the principles of interferometry and split-ring resonators (SRRs) to achieve high sensitivity and accuracy in non-contact displacement sensing. The study explores various configurations, including complementary Michelson and Mach-Zehnder interferometric setups, to convert phase changes into measurable amplitude variations, simplifying the detection process.

This research starts with an in-depth review of existing microwave sensors and their applications in humidity detection, material characterization, crack detection, and displacement measurement. It then establishes the theoretical basis for microstrip lines, directional couplers, and SRRs before designing and simulating a branch-line hybrid coupler (BLHC) optimized for phase analysis. The results confirm a linear phase response with a sensitivity of 12°/mm, demonstrating the sensor's precision in displacement sensing. To validate performance, full-wave simulations using ADS, CST, and HFSS were conducted, showing a displacement sensitivity of up to 3.6 dB/mm.

Experimental validation is conducted using fabricated prototypes, with measurements aligning closely with simulation results. The proposed sensor exhibits advantages such as compact size and robustness. Potential applications include structural health monitoring, biomedical sensing, and industrial automation. Future work may focus on miniaturization, multi-parameter sensing, and integration with wireless systems for real-time monitoring.

Acknowledgement

Firstly, I would like to express my profound gratitude to Prof. Maurizio Bozzi, who has always enlightened and inspired me throughout the research process.

I must mention my sincere thanks to Prof. Michal Mrozowski for his guidance and for sharing his knowledge, which has helped me grow both academically and professionally.

I extend my heartfelt appreciation to Prof. Marco Pasian for his insightful support.

I thank the Faculty of Engineering of the University of Pavia for the high quality of education.

It was an honor to conduct the research in University of Technology Gdansk.

Lastly, I extend my heartfelt gratitude to my family for their understanding, encouragement, and continuous support during this challenging academic journey.

List of Contents

List of Figures

List of Tables

List of Symbols and Acronyms

EM	Electromagnetic
VNA	Vector Network Analyzer
PCB	Printed Circuit Board
RF	Radio Frequency
MTEE	Microstrip T-Junction
MLIN	Microstrip Line
BLHC	Branch-Line Hybrid Coupler
SIW	Substrate-Integrated Waveguide
CPW	Coplanar Waveguide
DS-DGS	Dumbbell-Shaped Defected Ground Structure
MI	Michelson Interferometer
MZI	Mach-Zehnder Interferometer
SRR	Split Ring Resonator
CCRR	Complementary Curved Ring Resonator
ELC	Electric-LC
CST	Computer Simulation Technology
MATLAB	Matrix Laboratory
ADS	Advanced Design System
HFSS	High-Frequency Structure Simulator
FEM	Finite Element Method
MoM	Method of Moment
E-field	Electric field [V/m]
H-field	Magnetic field [A/m]
PVA	Poly Vinyl Alcohol
SMA Connector	Semi-precision Coaxial RF Connector

f_r	Resonance frequency [Hz]
ε_0	Electrical permittivity of free space [F/m]
ε_r	Relative permittivity
λ_g	Guided Wavelength [m]
α	Attenuation constant [Np/m]
β	Phase (Propagation) constant [rad/m]
v_p	Phase velocity [m/s]
Z_0	Characteristic impedance [Ω]
c_0	Speed of light in free space [m/s]
T	Transmission coefficient [dB]
Γ	Reflection coefficient [dB]

Chapter 1:

Introduction

Introduction

Sensors play an important role in modern technology by enabling the detection and measurement of various physical, chemical, and biological parameters. There has been increasing interest in utilizing radio frequency (RF) and microwave (MW) technology to develop various sensors, including those for humidity [1], [2], [3], [4], material characterization [5], [6], [7], crack detection [8], [9], [10], [11], temperature-pressure detection [12], displacement sensors [13], [14], [15], [16], [17], [18]. These sensors are widely used in industries such as automation [19], structural health monitoring [20], robotics [21], and biomedical engineering [22].

1.1 General Introduction

Microwave sensing has emerged as a powerful and versatile technique for the non-invasive detection and characterization of materials, leveraging the interaction of electromagnetic (EM) waves with matter to extract valuable information about its electrical, structural, or compositional properties. Due to its high sensitivity, rapid response, and potential for miniaturization, microwave-based sensors have found growing applications across diverse fields such as biomedical diagnostics, structural health monitoring, environmental analysis, and industrial process control. Fundamental phenomena such as resonance frequency shifts, phase variations, and scattering parameter changes form the basis of detection mechanisms, enabling accurate and real-time monitoring of dielectric changes in target materials. This thesis explores the principles, design methodologies, and practical implementations of microwave sensors, with a focus on optimizing their performance for specific sensing scenarios.
Displacement sensors are devices used to measure the movement or position of an object in relation to a reference point.
Traditional displacement sensors are classified into contact-based and non-contact-based types, like capacitive [23], and inductive sensors [24], ultrasonic [25], laser interferometers [26], have some drawbacks. They can be sensitive to environmental conditions, may wear out over time, and often have limited measurement ranges.

In recent years, microwave displacement sensors have gained significant attention due to their high accuracy, non-contact measurement capability, and ability to function in harsh environments[27]. These sensors utilize microwave

signals to detect movement based on Doppler shifts [28], frequency modulation techniques [13], [14], [29], or phase variations [15], [30], [31], [32].

1.2 Importance of phase variation analysis

Phase variation analysis is a fundamental technique in microwave sensing, as it allows for precise measurements of material properties, displacement, and other critical parameters. Unlike amplitude-based sensing, which is often susceptible to noise and attenuation, phase-based measurements provide a more robust and reliable approach to detecting subtle changes in a target medium. This makes phase variation analysis an essential tool in applications such as biomedical diagnostics, structural health monitoring, and subsurface imaging.
Interferometry, which exploits the interference patterns of EM waves to detect minute changes in phase or distance, plays a crucial role in high-precision sensing applications. The two main types of Mach-Zehnder and Michelson interferometers offer distinct configurations for manipulating signal paths and measuring phase differences. Each design has its own merits depending on the sensing context: for example, Mach-Zehnder setups are well-suited for integrated sensor systems, while Michelson configurations are often favoured for their simplicity and sensitivity in free-space measurements. Additionally, a comparison between different types of interferometry measurement strategies reveals important trade-offs; while single-frequency systems offer fast response times and simpler electronics, sweep-frequency systems provide broader characterization capabilities and higher resolution. Single-frequency operation allows for real-time and continuous monitoring with relatively simple circuitry, whereas sweep-frequency operation enables detailed characterization of frequency-dependent behaviors and can be used to extract dielectric properties through curve fitting or inversion algorithms.

1.3 Work Focus

This thesis aims to design and develop a microwave sensor that utilizes phase variation analysis to enhance detection capabilities. The key objectives of this research include:

1. Investigating the principles and theoretical background of microwave sensor technology.

2. Design and implementation of a novel microwave sensor system optimized for phase variation analysis.
3. Developing an experimental setup to validate the sensor's performance.
4. Evaluating the effectiveness of the designed sensor by analysing experimental results.
5. Comparing the developed system with existing technologies to highlight improvements and potential applications.

1.4 Structure of the thesis

This thesis has been structured into five chapters. The following itemized list provides an in-depth summary of each chapter:

- **Chapter One: Introduction**

This chapter has provided the summary of background and motivation of the research study, the aim and objectives, contribution to knowledge from this study and organisation of the thesis.

- **Chapter Two: Literature Review**

It provided comprehensive documental research, detailing previous research on the structures of the microwave sensors and phase variation analysis. Additionally, the design process for both split ring resonator and Interferometric Microwave Sensors is explained.

- **Chapter Three: Material and Methods**

Theoretical background for microstrip lines, Branch-Line Hybrid Coupler, and SRR design, along with mathematical modeling of phase variation and interferometry is fully explained.

- **Chapter Four: Results and Discussion**

This chapter presented the BLHC and SRR design and validation displacement sensor performance, and a comparative evaluation of Michelson and Mach-Zehnder interferometric sensors, supported by experimental results and their

alignment with simulation methodologies using ADS, CST, HFSS, and MATLAB. Finally, tables of comparison are elaborated the results and dimensional details.

- **Chapter Five: Conclusion and Future work**

This chapter summarizes key findings, discusses limitations and potential improvements, and explores future research directions and applications, ensuring a comprehensive and cohesive progression from theoretical foundations to practical implementation.

Chapter 2:

Literature Review

Literature Review

This chapter presents a literature survey on different passive microwave sensors that have been introduced for non-contact sensing. Passive microwave planar sensors will be described in this section. Section 2.5 will focus on just displacement microwave planar sensors.

2.1 Applications for RF/Microwave Sensors

Sensors play a vital role in today's technology-driven world, acting as the backbone for gathering crucial data across countless applications. They're designed to detect and measure a wide range of physical, chemical, and biological factors: like temperature, humidity, movement, and material characteristics, making them indispensable in industries, environmental monitoring, healthcare, and scientific research. Recently, Radio Frequency and microwave technologies have become a major focus in sensor innovation. Their unique ability to interact with materials in non-invasive ways offers exceptional sensitivity and precision. These sensors work by using EM waves to pick up on environmental changes, which are then converted into measurable data. In this section, we'll explore the basics of RF and microwave sensors, how they function, and the diverse ways they're being used across different fields.

2.2 Humidity Sensors

Humidity sensing using microwave detection has become an active area of research due to its non-invasive, high-sensitivity, and fast response advantages. Humidity sensors based on microwave technology typically rely on the interaction of EM waves (microwave or RF signals) with a material that changes its electrical

properties (like dielectric constant or conductivity) when exposed to moisture. These changes, often measured as a shift in resonance frequency or impedance, can then be used to determine the level of humidity.

This paper [21] explores how gelatin and poly vinyl alcohol (PVA) perform as humidity-sensitive coatings for a microwave sensor. The researchers used a special type of capacitive sensor and tested how well each material responded to changes in humidity. Gelatin, which comes from animal collagen, showed a stronger and more noticeable reaction to humidity shifts compared to PVA, especially at lower humidity levels. By analyzing how the materials affected the sensor's properties, the study found that gelatin had a greater impact on detecting moisture changes. These results suggest that gelatin could be a better option for making highly sensitive humidity sensors in microwave applications.

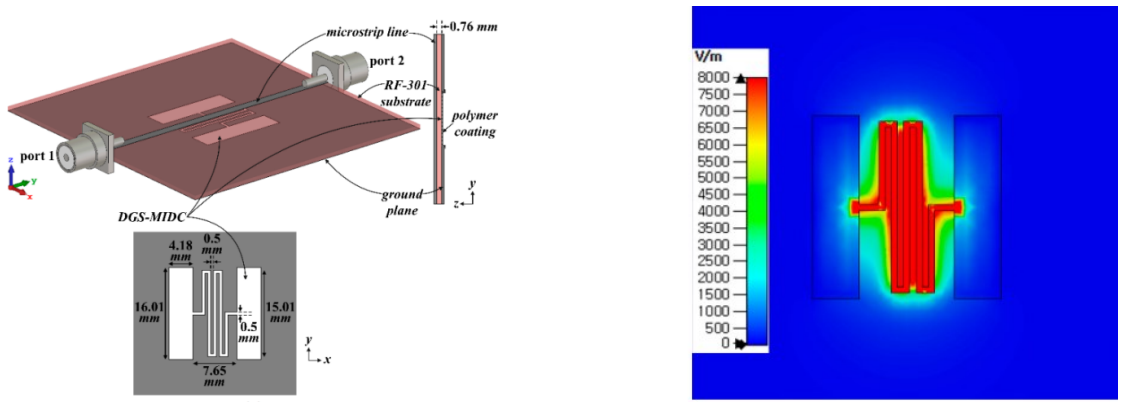

(a) (b)

Figure 2-1 a) General structure of a DGS-MIDC sensor, b) Electric field of simulated sensor [21].

The researchers developed a highly sensitive two-port microwave sensor using a specialized DGS-MIDC structure on a compact RF-301 substrate (50 mm × 50 mm). This design helps focus the electric field (E-field) along the microstrip transmission line, as illustrated in Figure 2.1(a). The sensor naturally exhibits the band-stop behavior at specific frequencies, but when a humidity-sensitive polymer is applied to its surface, the resonance frequencies shift based on changes in the polymer's

properties under different humidity levels. The E-field is primarily concentrated in the gaps between the interdigital fingers, which plays a crucial role in sensing humidity variations, as shown in Figure 2.1(b).

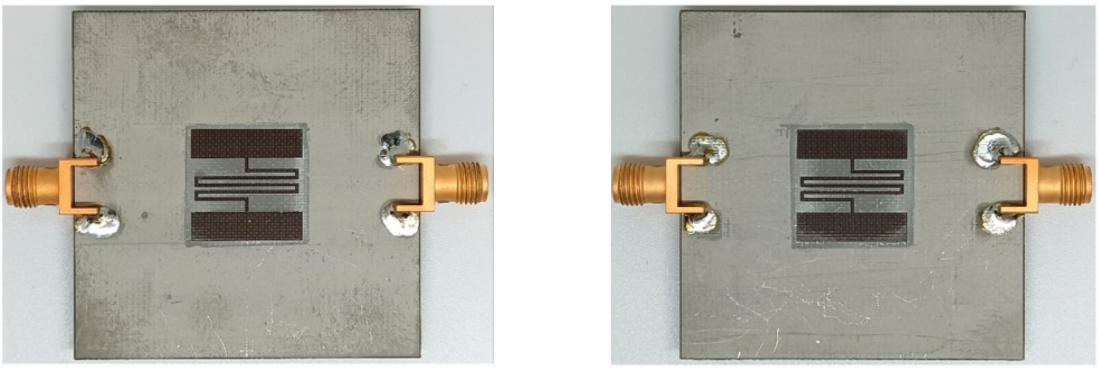

(a) (b)

Figure 2-2 Fabricated structures of a) Poly vinyl alcohol, b) Gelatin [21].

Figure 2-2 (a) and (b) show the fabricated microwave sensors with DGS-MIDC coated with PVA and gelatin, respectively, on an RF-301 substrate. The PVA (polymerization degree: 1500, saponification: 99 mol%) was sourced from Yakuri Pure Chemicals, Japan, while the type A gelatin (300 g Bloom, from porcine skin) was supplied by Sigma-Aldrich, USA.

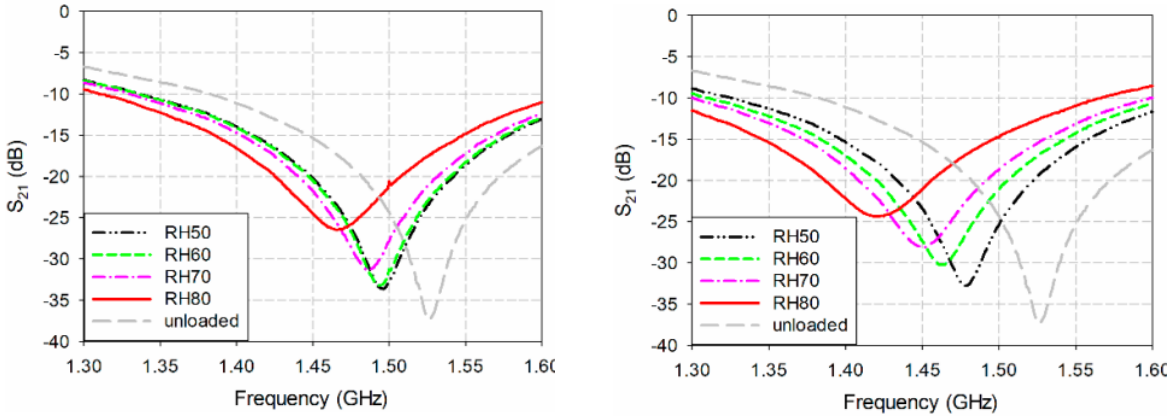

(a) (b)

Figure 2-3 Measured graphs of a) PAV, b) Gelatin humidity sensor [21].

The S21 characteristics of the microwave humidity sensors coated with PVA and gelatin, shown in Figure 2-3(a) and (b) were measured and compared across different humidity levels, respectively. Under unloaded conditions (without a polymer coating), the first resonance frequency and magnitude level were 1.526 GHz and −37.38 dB, respectively.

2.3 Material Characterization Sensors

This type of sensor uses microwave signals to study and identify different material properties, like how well they conduct electricity, their composition, or their dielectric constant (how they respond to E-fields). These sensors are popular because they're quick, highly sensitive, and don't damage the materials they test. That makes them perfect for a wide range of uses, from chemistry labs and healthcare to food quality checks and industrial production. They're also incredibly versatile, working with everything from liquids and solids to gases.

The paper [7] presents a compact, highly sensitive microwave sensor that measures material permittivity (ε) using a complementary curved ring resonator (CCRR). The sensor creates a strong magnetic field (H-field), interacting with materials and causing a frequency shift. By tracking this shift, it accurately calculates permittivity. Tested through simulations and real-world experiments, the sensor showed high precision and resolution, making it a reliable tool for material analysis in microwave applications.

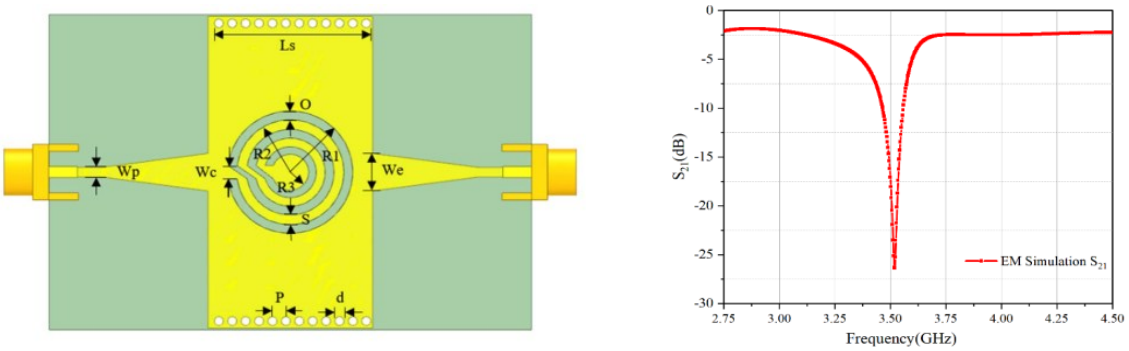

(a) (b)

Figure 2-4 a) General shape of the Material Characterization sensor, b) Transmitted coefficient simulation graph [7].

As shown in Figure 2-4(a) By adding two rows of metal through-holes on both sides of the substrate, the sensor forms a substrate-integrated waveguide (SIW) structure along with a conical transmission line. A quick look at Figure 2-4(b) shows that in its unloaded state, the sensor operates at a resonance frequency of 3.51GHz with a transmission coefficient of -27.5dB and a bandwidth of 105MHz. To analyze its performance, simulations were conducted using different loss angle tangent values while keeping the real part of the dielectric constant at 1.

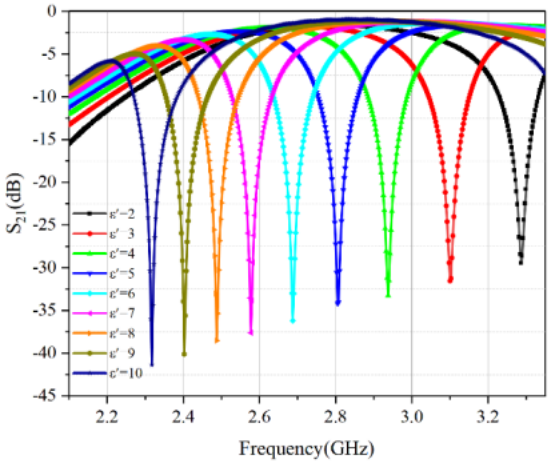

Figure 2-5 Transmitted simulation for different dielectric constants [7].

As shown in Figure 2-5 when the sensor is loaded with a material whose dielectric constant increases from unloaded to ε’ = 10, the resonance frequency gradually decreases. It shifts from 3.51GHz to 2.31GHz, resulting in a total frequency change of 1.2GHz, demonstrating the sensor’s sensitivity to permittivity variations.

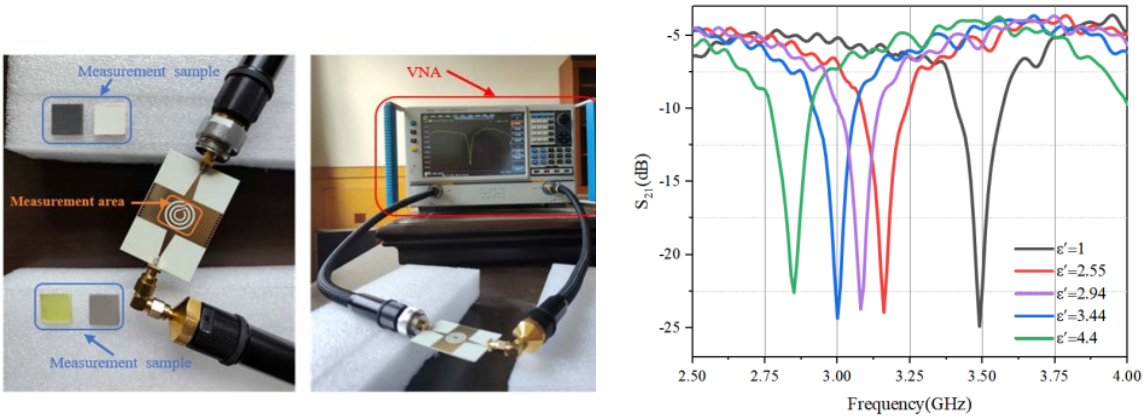

(a) (b)

Figure 2-6 a) Fabricated sensor with Measurement Setup, b) Measured graph for various dielectric constants [7].

The fabricated sensor in Figure 2-6(a) was equipped with SMA connectors at both ends, allowing it to be connected to a vector network analyzer for measuring the resonance frequency. Figure 2-6(b) shows the complete measurement setup, the measured resonance frequency shifts after loading four different materials are 330 MHz, 410MHz, 480MHz, and 630MHz, respectively. These shifts highlight the sensor's high resolution and its strong ability to distinguish materials with varying permittivity values.

The study explores how structural variations impact measurement accuracy and demonstrates that the optimized CCRR design enhances E-field intensity, improving sensitivity. Testing with four substrate materials confirms the sensor's high precision, even for materials with small permittivity differences. Future research will focus on adapting this design for liquid concentration sensing and solution differentiation applications.

2.4 Crack Detection Sensor

This study [8] presents a crack detection sensor based on a dumbbell-shaped defected ground structure (DS-DGS) in microstrip technology. Featuring an etched pattern on the ground plane, the sensor is easy to fabricate and interacts

effectively with EM fields. It detects cracks by monitoring shifts in resonance frequency when placed over a metallic surface. While it is most sensitive to cracks perpendicular to the inductive strip, detection can be improved for other orientations by increasing the inductive strip length. Using a larger defect design, the sensor enhances sensitivity and offers a promising non-invasive solution for crack detection in metallic structures.

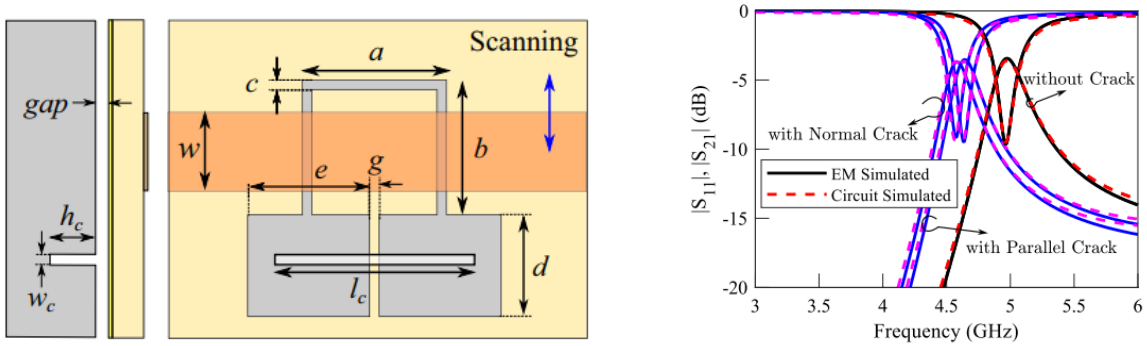

(a) (b)

Figure 2-7 a) Dumbbell-shaped metallic crack detection structure, b) Simulated Reflection and Transmitted results [8].

By optimizing these dimensions, the sensor shown in Figure 2-7(a) achieves equal sensitivity to cracks in both parallel and orthogonal directions and can also detect cracks at various angles. To demonstrate its effectiveness shown in Figure 2-7(b), a square-shaped defect design was tested using full-wave EM simulations. In essence, this sensor enhances crack detection by refining its structure for improved accuracy across different orientations.

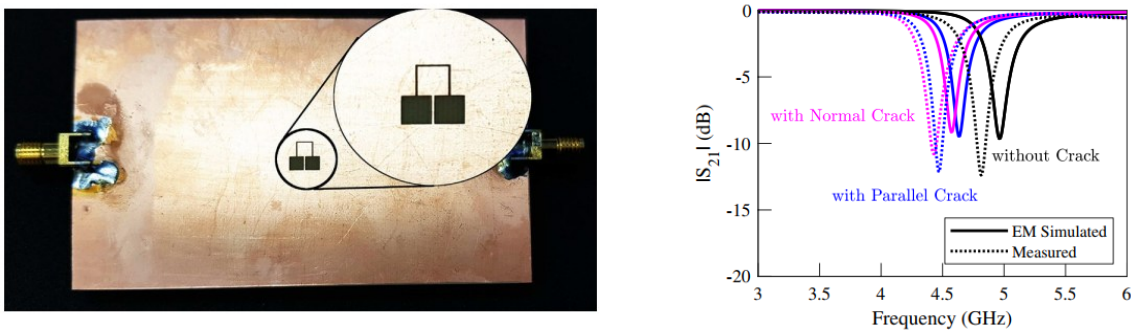

(a) (b)

Figure 2-8 a) Fabricated PCB of DS-DGS, b) Comparison of EM Simulated and Measured Results [8].

To validate the design, a prototype of the folded dumbbell-shaped sensor with square defected areas, as illustrated in Figure 2-8(a), was fabricated and tested to detect cracks in various orientations. As shown in Figure 2-8(b), the prototype matches the simulated structure in dimensions and materials. Measured and simulated transmission coefficients were compared for faultless and cracked metal surfaces. While a slight frequency shift occurred, likely due to fabrication tolerances, the consistent resonance shifts in both measurements and simulations confirm the sensor's effectiveness in crack detection.

2.5 Displacement Sensors Based on Microwave Technology

2.5.1 Amplitude-Variation Based

A non-contact microwave rotation sensor detects and measures rotational movement using microwave signals. This lightweight microwave tilt sensor provides a practical and efficient way to measure inclination. It is designed using a split-ring resonator (SRR) loaded microstrip line (MLIN), which takes advantage of the symmetrical properties of SRRs. As the sensor tilts, the depth of the notch in its reflection characteristic changes, allowing for accurate tilt detection. Its small size and light weight make it easy to integrate into various applications. Additionally, since it operates at a single frequency, it requires only a simple power meter for reading, making it both cost-effective and easy to use. EM simulations confirm their reliability in delivering precise tilt measurements across a broad range of angles [33].

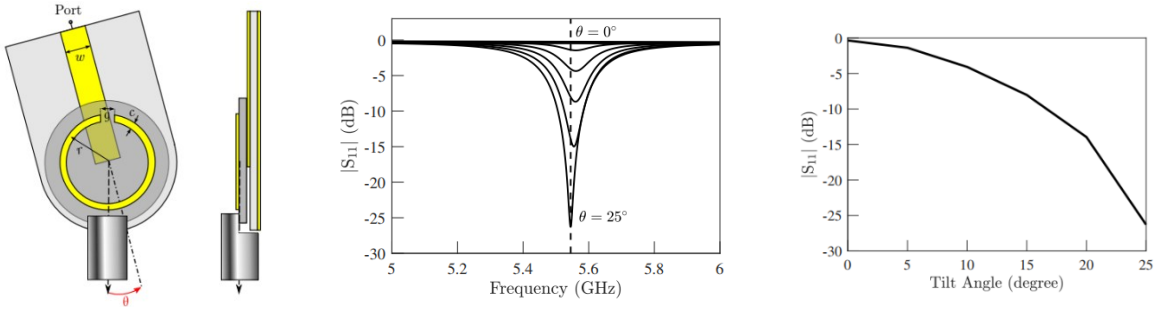

(a) (b) (c)

Figure 2-9 a) Rotation sensor scheme, b) Resonance frequency of the reflection coefficient for different angels, c) Comparing normalized simulated transmission coefficients of the proposed sensor [33].

As outlined in Figure 2-9(a), the sensor is designed with two substrates, each playing a crucial role in its operation. The first substrate features an open-ended microstrip line on its top side, while its underside is entirely covered with a copper layer, forming the ground plane. On top of the second layer, there's a SRR placed at the end of the MLIN. This second layer sits above the first one and is designed to freely rotate around its axis. It's also connected to a hanging metal block that acts like a pendulum, allowing it to naturally swing and align itself with gravity. This structural design enables precise tilt sensing by responding to changes in orientation. When the sensor is functioning, a full reflection is seen across the frequency range of interest shown in Figure 2-9(b). However, if the structure is tilted at any angle, even slightly, it causes a notch to appear in the reflection coefficient. According to the EM simulations, larger tilt angles cause a stronger interaction between the SRR and the MLIN, which leads to a deeper notch in the reflection. In essence, the simulation results show that the depth of this notch can effectively be used to measure the tilt or inclination angle.

A microwave inclinometer using an SRR-loaded open-ended MLIN has been introduced. As seen in the Figure 2-9(c), it has been demonstrated that when the symmetry of the SRR aligns with the MLIN, the SRR remains inactive, and no notch appears in the reflection coefficient. However, when the structure is tilted, breaking its symmetry, a notch emerges at the SRR's resonance frequency. The

depth of this notch is directly related to the tilt angle, allowing the sensor to effectively measure inclination. This proposed sensor offers notable advantages, including high sensitivity, a wide measurement range, compact design, and light weight.

2.5.2 Frequency-Variation Based

Microwave resonance frequency-variation based displacement sensors in reflective mode offer a highly sensitive and adaptable solution for detecting movement. These sensors work by measuring shifts in resonance frequency, which change as an object moves. To improve accuracy, a tapered metallic patch is used to enhance capacitive properties, ensuring better linearity and a wider dynamic range.

The design [13] includes a coplanar waveguide (CPW) with a resonator, where a movable dielectric slab sits above the capacitive patch. As this slab shifts, it alters the capacitance, causing variations in frequency that indicate displacement. Detailed circuit modelling and EM simulations help analyse the sensing process, demonstrating the sensor's ability to detect both the amount and direction of movement. Additionally, this approach can be extended for two-dimensional displacement sensing. The effectiveness of this design is further supported by prototype fabrication and testing, confirming its practical application.

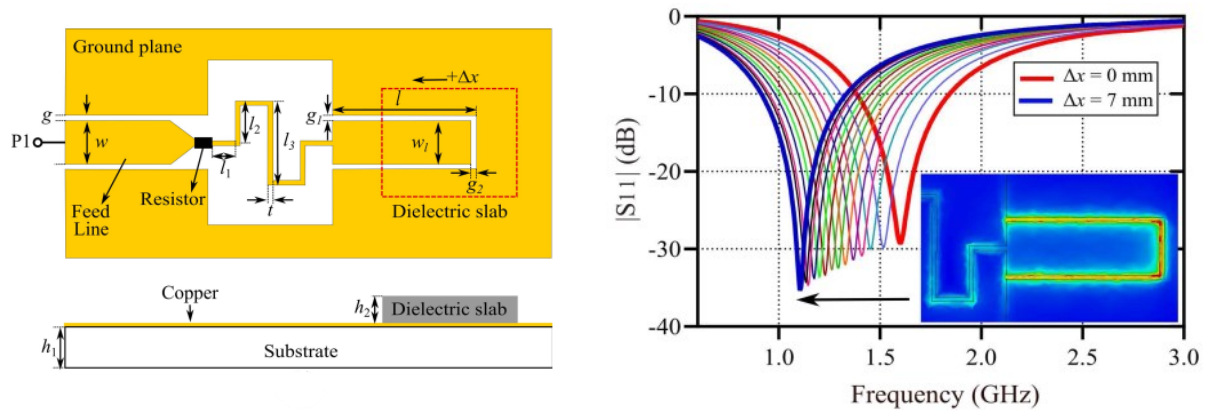

(a) (b)

Figure 2-10 a) General configuration for rectangular dielectric slab of coplanar waveguide displacement sensor, b) Simulated results of the CPW sensor [13].

The proposed reflective mode displacement sensor in Figure 2-10(a) operates using a coplanar waveguide (CPW) structure with a feedline connected to a series RLC resonator. The inductor is formed by a narrow, meandered metallic trace, while a rectangular patch serves as the capacitor, interacting with the CPW ground plane to create edge capacitance. To enhance inductance, the CPW ground metallization around the trace is cleared. A resistor is placed between the feedline and the inductor to ensure proper termination at resonance, creating a noticeable notch in the reflection coefficient. A movable dielectric slab positioned above the patch alters the capacitance as it shifts, modifying the resonance frequency. This frequency change can be tracked through the reflection coefficient, allowing displacement measurement. At the start of displacement displayed in Figure 2-10(b), the resonance frequency shifts quickly shown in, but this change slows down as displacement increases, creating a nonlinear response. This happens because the E-field is highly concentrated at the edge of the capacitive patch, making it very sensitive to initial changes.

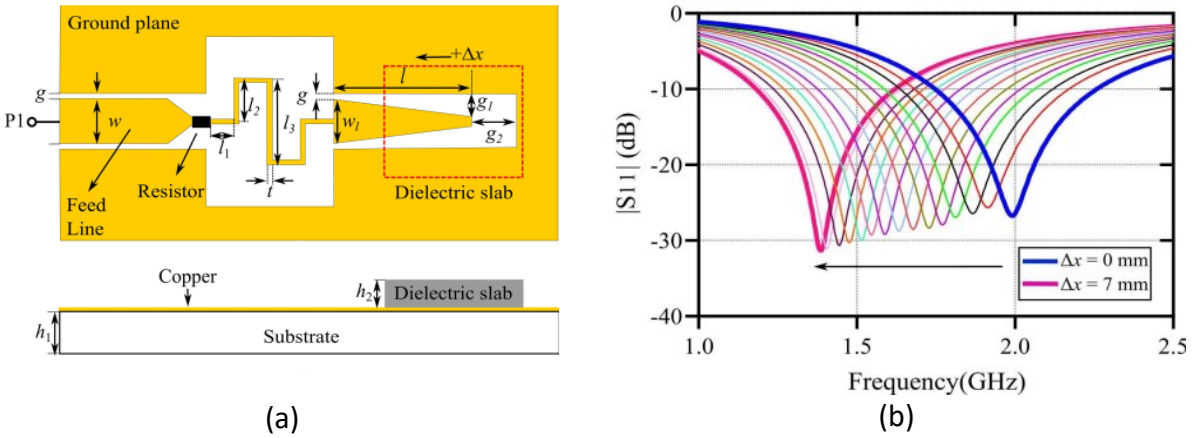

(a) (b)

Figure 2-11 a) General Structure for Triangular Dielectric Slab of CPW Displacement Sensor, b) Simulated Results of the CPW sensor [13].

To improve linearity, the capacitive gap represented in the Figure 2-11(a) is tapered, starting wider and gradually narrowing. This evens out the sensitivity, reducing sharp changes early on while enhancing response at larger displacements. Simulations confirm that this approach improves accuracy and consistency in measuring displacement outlined in Figure 2-11(b).

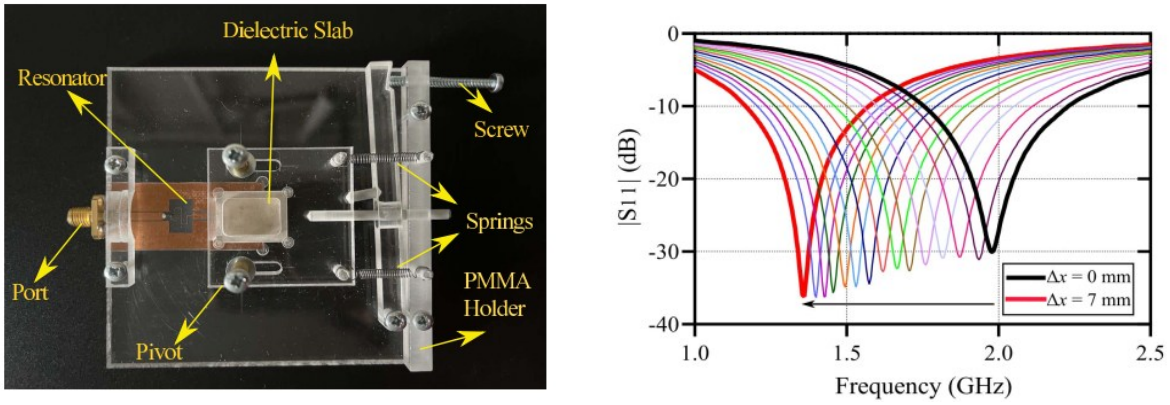

(a) (b)

Figure 2-12 a) Fabricated Triangular Dielectric Slab Setup with Resonator, b) Measured S_{11} magnitudes for the proposed linearity improved reflective mode for different displacements [13].

A displacement sensor that works using resonance in reflective mode shown in Figure 2-12(a) has been developed and tested. It measures movement by detecting changes in resonance frequency, which vary depending on how far something has moved. Experimental tests, shown in Figure 2-12(b), confirm that this method is effective. The close match between the simulation results and the

data from the actual prototype proves that the design and theory behind the sensor are solid, demonstrating its accuracy and reliability.

2.5.3 Phase-Variation Based

This study [31] introduces a novel microwave displacement sensor designed for high linearity, particularly in breath rate monitoring. The sensor comprises a stationary reader (a transmission line with a matched load) and a movable tag (a dielectric slab with an electric LC resonator). As the tag shifts along the reader's axis at a fixed vertical distance, magnetic coupling causes the reflection phase to change linearly with displacement. The sensor's potential for breath monitoring was explored, demonstrating its ability to track chest and abdominal movements via a belt-based prototype.

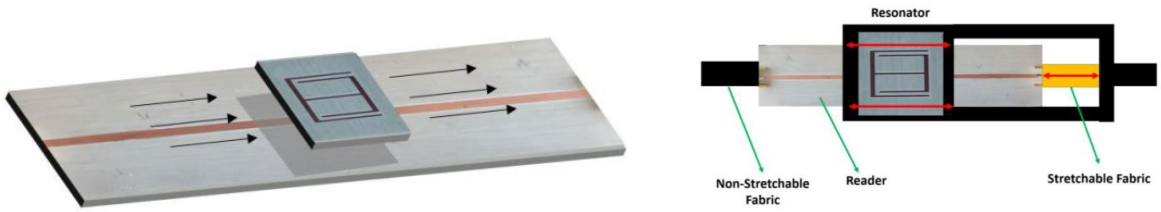

Figure 2-13 Perspective view of the proposed reflective-mode phase variation displacement sensor [31].

The sensor shown in Figure 2-13 consists of a static reader, a transmission line with a matched load, and a movable tag, an ELC resonator etched in a dielectric slab. For proper function, the resonator moves along the reader's axis, aligning its magnetic wall with the line. This orientation enables strong magnetic coupling, as counter H-fields excite the resonator. To ensure effective operation, the feeding signal's frequency must match the resonator's fundamental resonance. In simpler terms, the sensor works by leveraging precise alignment and frequency tuning to achieve accurate displacement detection.

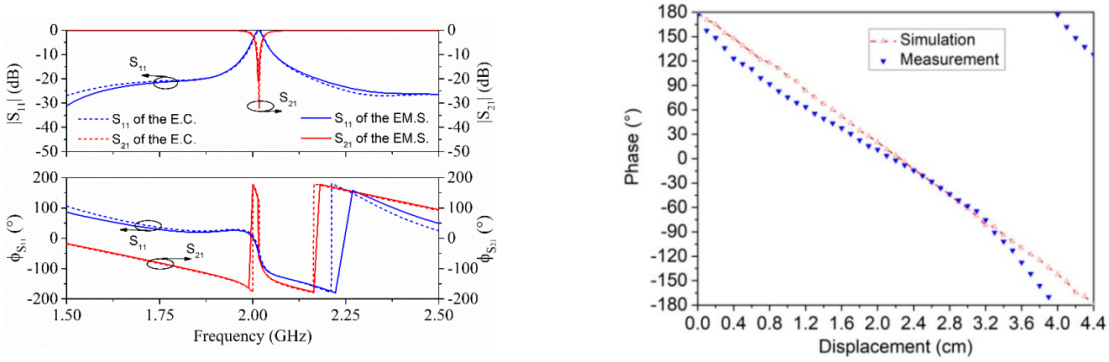

(a) (b)

Figure 2-14 a) Magnitude and phase of S_{11} and S_{21} for the structure introduced with the location of the resonance element as indicated in the text, b) Variation of the phase of the reflection coefficient with the displacement as inferred from EM simulation and measurement [31].

As presented in Figure 2-14(a), which displays the magnitude and phase of S_{11} and S_{21} at central frequency, shows how much microwave signal is reflected and transmitted and how the sensor responds to these physical changes, such as those caused by breathing and the phase of the reflection coefficient at the resonance frequency was analyzed as the ELC resonator moved along the line, with an indicated air gap, using full-wave EM simulation through ANSYS HFSS software. Results shown in Figure 2-14(b) indicate that the phase of the reflection coefficient changes linearly from its initial position, with the output dynamic range spanning 2π, representing a complete cycle. In simpler terms, the simulations and the experimental data confirmed that the sensor's response behaves predictably as the resonator shifts.

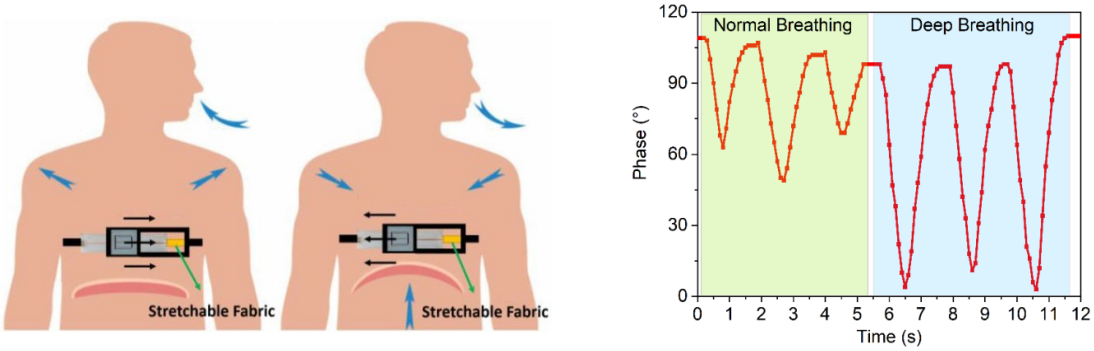

(a) (b)

Figure 2-15 a) Breath rate sensor concept, b) Phase of the reflection coefficient recorded using a VNA while a volunteer wearing the belt-based sensor breaths as indicated [31].

The breath rate sensor comes with a comfortable belt that wraps securely around the person's abdomen or chest, as illustrated in Figure 2-15(a). The belt has a stretchy section which is flexible that expands when the person breathes in and contracts when they breathe out, moving naturally with their breathing. Attached to the non-stretchy part of the belt is the sensor's reader, which has rails guiding a movable piece holding the ELC resonator board. This design keeps a small, steady gap between the parts. The movable section is connected to the stretchy fabric on the other side, allowing smooth, rhythmic movement between the reader and the tag that matches the wearer's breathing pattern perfectly.

To test the experiment, the belt was placed on a volunteer who first took three normal breaths, followed by three deep breaths. Using a vector network analyzer (VNA), the phase of the reflection coefficient was measured, with data recorded every 0.1 seconds. The results, displayed in Figure 2-15(b), clearly captured the volunteer's breathing pattern.

2.5.4 Phase-Variation and Interferometry Based

This subject [32] introduces displacement sensors based on a microstrip loaded with split ring resonators (SRRs), utilizing the phase of the reflection coefficient for sensing. A differential version is also proposed, offering higher sensitivity and a reference zero for better alignment. Additionally, an interferometry-based approach is explored to convert phase changes into amplitude variations, simplifying measurement. Validation is conducted through EM simulations and further confirmed by fabricating and testing a prototype. These findings highlight the potential of SRR-loaded transmission lines for precise displacement sensing.

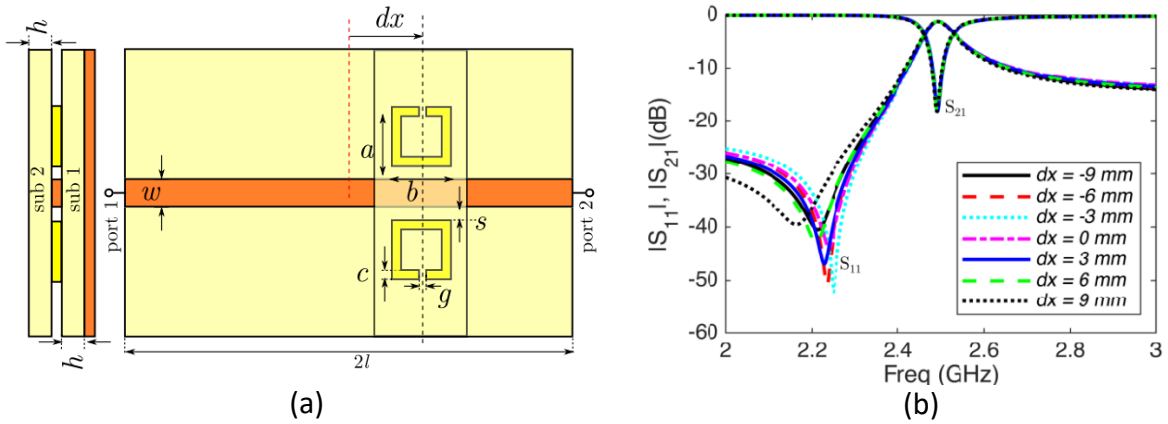

(a) (b)

Figure 2-16 a) Proposed structure for displacement sensing, b) Simulated magnitude of the transmission and reflection coefficients of the proposed sensor versus frequency for different values of displacement dx [32].

This section introduces the main concept of the proposed displacement sensor. As shown in Figure 2-16(a), the design consists of two stacked substrates: the first contains a MLIN and ground plane, while the second holds a pair of split ring resonators (SRRs). When the second port is matched to the impedance, signals are absorbed at all frequencies except the SRRs' resonance frequency, where they are reflected as illustrated in Figure 2.16(b).

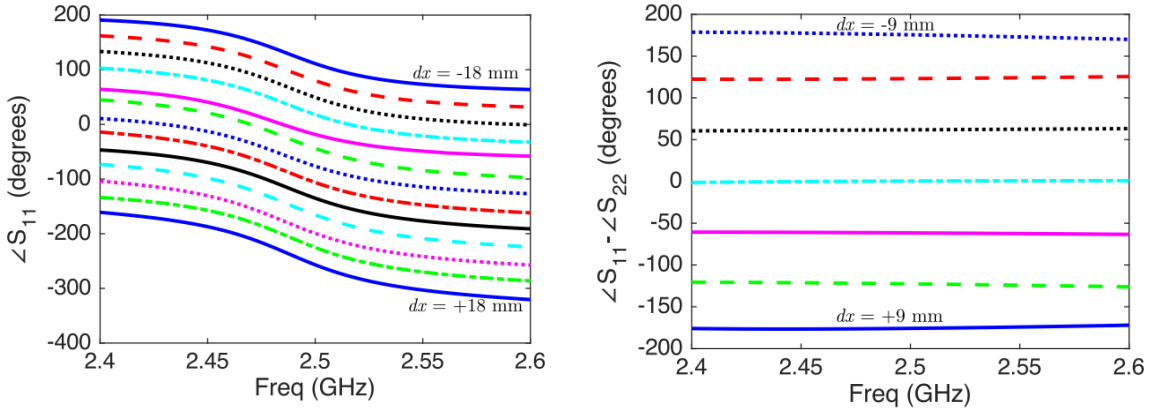

(a) (b)

Figure 2-17 a) Simulated phase of the reflection coefficient, b) Simulated phase difference [32].

At the initial position, when the SRRs are symmetrically aligned with the microstrip's input and output ports, the reflected signal's phase follows a specific relationship, determined by the microstrip's length and phase constant which is $\angle S_{11} = -2\beta l$. Figure 2-17(a) illustrates the simulated phase of the reflection

coefficient at port 1 across different frequencies for displacement values ranging from -18 mm to 18 mm. The sensor can also operate as a two-port structure, using the phase difference ($\Delta\varphi = \angle S_{11} - \angle S_{22}$) to measure displacement. Figure 2-17(b) presents the simulated phase difference for displacements ranging from -9 to 9 mm in 3 mm steps. Unlike the frequency-dependent results in figure 2-17(b), this phase difference method remains consistent across frequencies, as indicated by the straight lines.

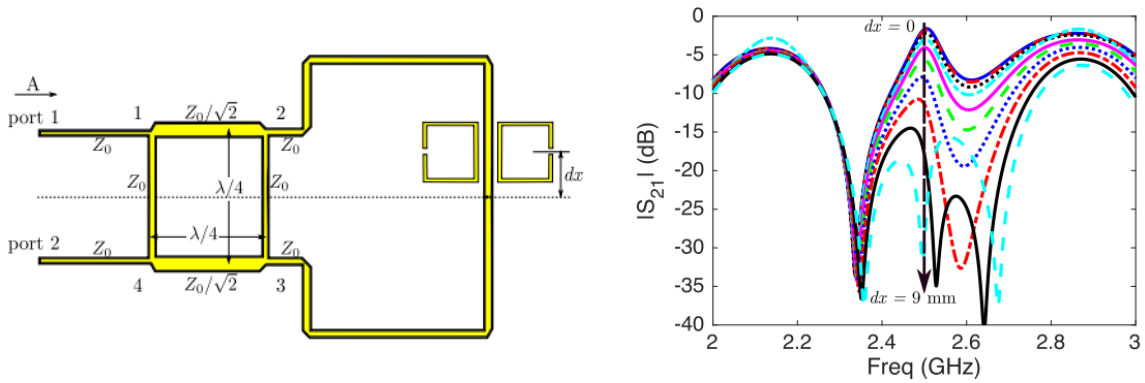

(a) (b)

Figure 2-18 a) Proposed sensor between two output ports of a BLHC, b) Simulated amplitude of transmission coefficient for different values of displacement dx [32].

While measuring phase difference has its benefits, it can also be a bit challenging. To simplify the process, this section explores the use of microwave interferometry. To get started, the sensor is connected between the two output ports of a branch-line coupler, as shown in Figure 2-18(a). Figure 2-18(b) shows the simulated transmission coefficient for different displacement values. As expected, S_{21} hits its highest amplitude when *dx* is zero. As the displacement grows, the amplitude of S_{21} slowly drops at the specified frequency.

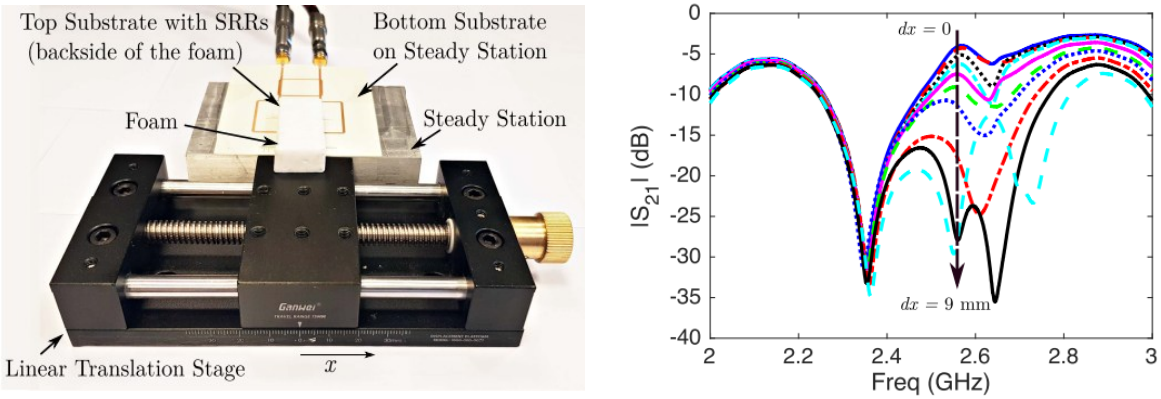

(a) (b)

Figure 2-19 a) Measurement setup for accurate adjustment, b) Measured amplitude of the transmission coefficient for different values of displacement dx [32].

The displacement sensor built and tested with a branch-line coupler. Figure 2-19(a) shows the prototype where increasing *dx* causes the amplitude of the transmission coefficient to drop at the SRRs' resonance frequency. The measured results presented in Figure 2-19(b) match the simulations quite well, though there's a small shift to 2.54GHz because of minor variations during fabrication.

Chapter 3:

Material and Methods

3.1 Concept of Distance Measurement with Interferometry

Interferometric distance measurement is a highly accurate method that relies on optical interference in which, it splits a beam of light (EM wave) into two paths, reflects them back, and then recombines them to produce interference patterns. When the measurement beam reflects off a target, changes in its position modify the optical path length, causing a phase shift when it recombines with the reference beam demonstrated from Figure 3-1. By examining the resulting interference pattern, distance changes can be measured with extreme precision, down to nanometers or picometers.

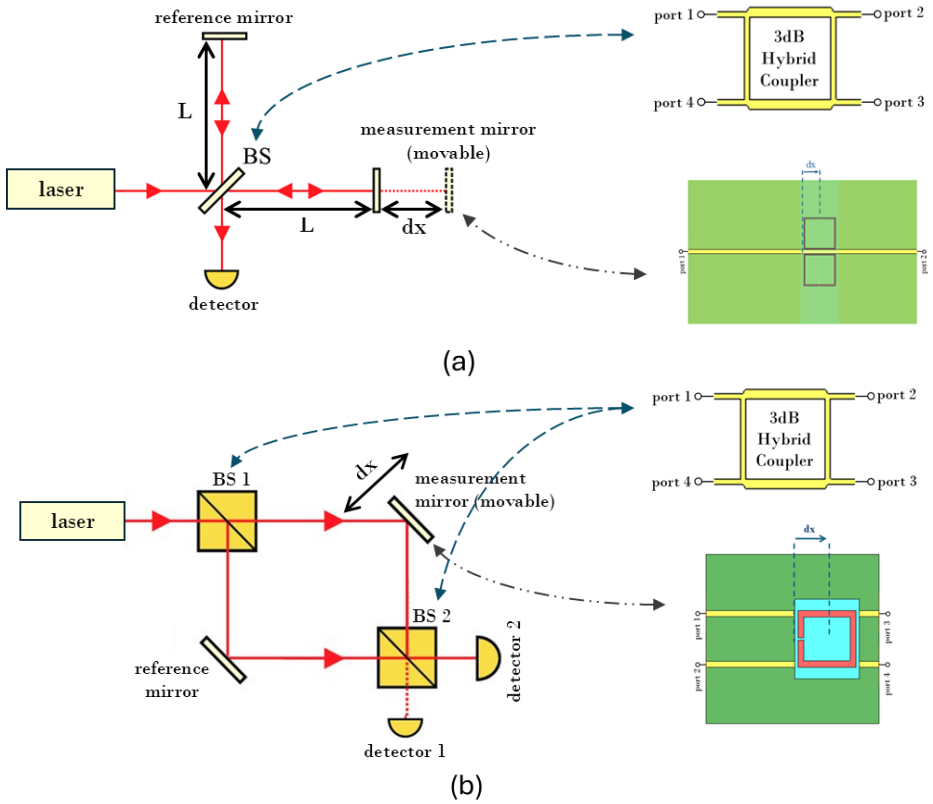

Figure 3-1 a) Michelson interferometers, b) Mach–Zehnder interferometer schematics.

In this chapter the theoretical background of the planar microstrip structures used in microwave displacement sensor based on phase variation and interferometry are described. In the context of microwave sensing, interferometric techniques provide a highly sensitive method for detecting small phase shifts, path length variations, or dielectric changes in a sample. Two of the most widely used configurations in this domain are the Mach-Zehnder interferometer (MZI) and the Michelson interferometer (MI).

As Shown in the Figure 3-2, Block diagrams of Michelson and Mach-Zehnder interferometers demonstrating the interferometric configurations used to realize phase-sensitive microwave sensor structures are discussed.

Generally, the Michelson interferometer, in contrast, operates based on reflection rather than transmission. It splits the incoming signal into two beams, each directed toward a separate arm and reflected by mirrors or reflectors. The beams then recombine at the splitter, where their interference pattern depends on the relative path lengths of the two arms. This setup is generally more compact and mechanically simpler for free-space measurements and is sensitive to changes in the optical (or electrical) path length, making it ideal for applications such as displacement sensing or surface profiling.

Also, the Mach-Zehnder interferometer consists of two signal paths or arms: a reference arm and a sensing arm. An input signal is split into these two paths using a 3dB coupler. The sensing arm typically interacts with the material or environment under test, while the reference arm remains unaffected. The two signals are then recombined, and any phase difference between them caused by the presence or change in the sample produces constructive or destructive interference at the output. This configuration is highly versatile and particularly well-suited for planar or integrated structures, including microstrip and waveguide implementations, due to its linear geometry and ease of integration with other components.

Moreover, designing different types of SRR which is essential to create a linear planar sensor are introduced.

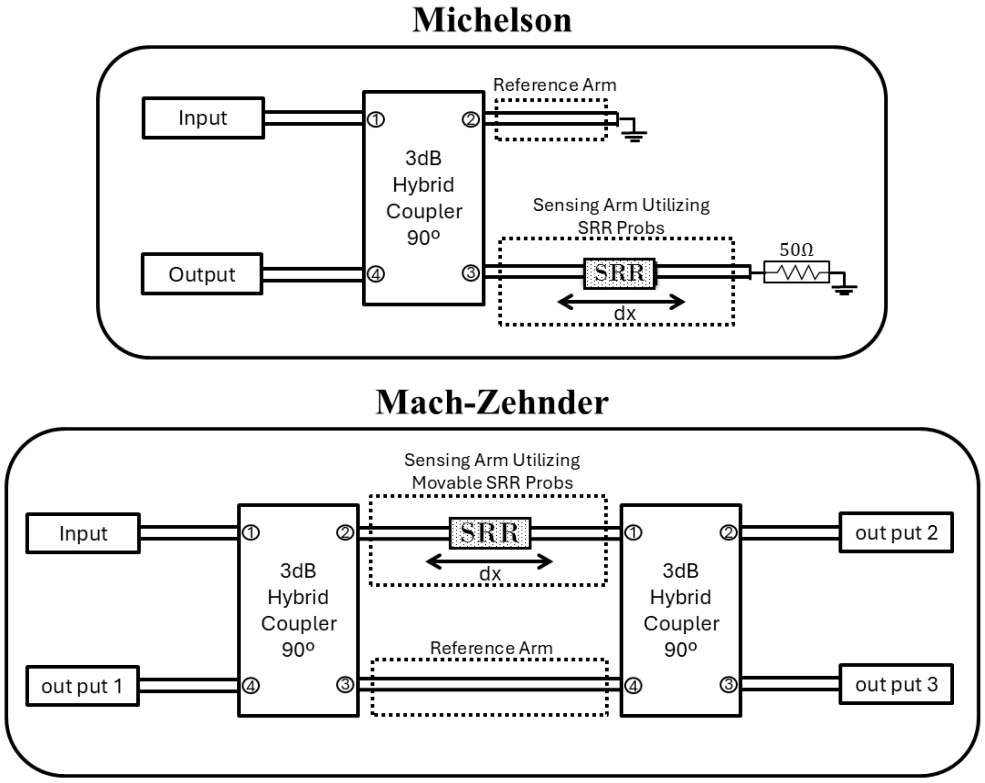

Figure 3-2 Block diagrams of Michelson and Mach-Zehnder interferometers.

In this thesis, a complementary modification of the Michelson and Mach-Zehnder interferometers have been proposed. In which, for MI the sensing and referenced arms are connected to each other and the phase difference is measured according to symmetry plane (dx=0mm) illustrated in Figure 3-3. This configuration provides inherent common-mode noise rejection and an intrinsic alignment reference at dx=0mm where $\Delta\varphi$=0; Unlike conventional MI designs, this system exploits complementary phase shifts in reflection coefficients. Also, for MZI a new modification known as push-pull MZI has been evaluated.

The push-pull MZI illustrated in Figure 3-3, employs symmetric differential interferometry, complementary path-length changes are intentionally induced in both arms, generating opposing phase shifts. This doubles the effective phase difference at the output. Critically, the push-pull configuration intrinsically rejects

common-mode environmental noise by cancelling symmetric disturbances across both arms, while simultaneously enabling absolute displacement measurement through the differential output. This architecture offers critical advantages for high-precision metrology, where optimization of signal-to-noise characteristics are essential.

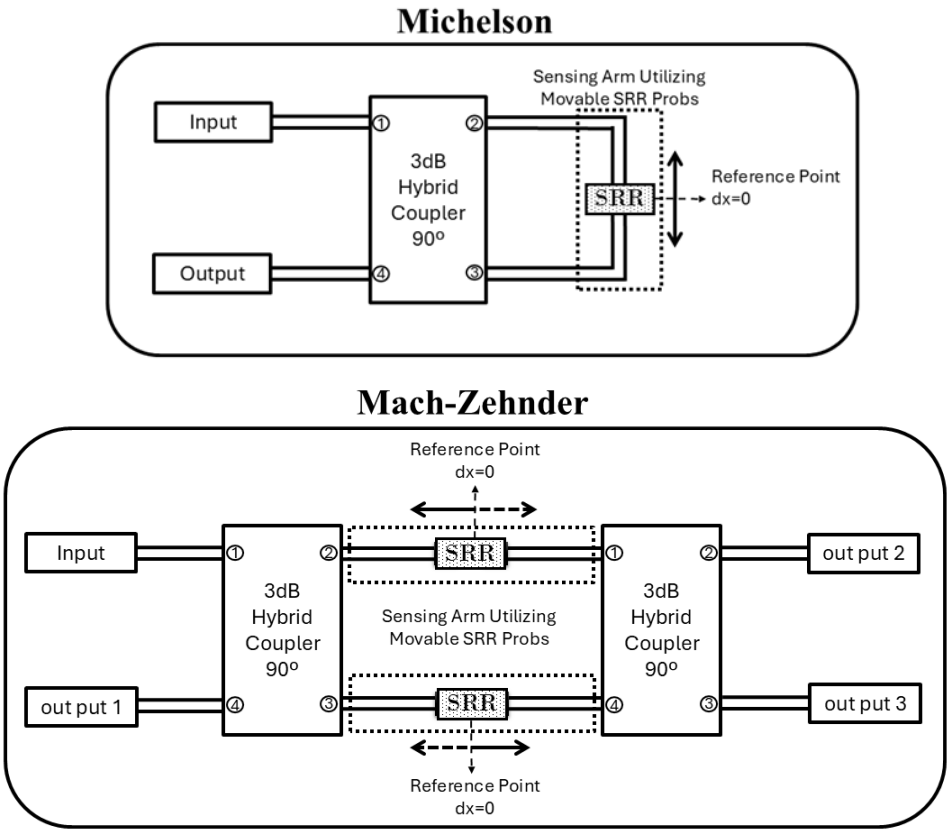

Figure 3-3 Block diagrams of Complementary Michelson and Mach-Zehnder interferometers.

3.2 Realization of 3dB Couplers and Reflecting Mirrors

In practical implementations of interferometric microwave sensors, the realization of key components such as 3 dB couplers and reflecting mirrors is crucial for ensuring efficient signal splitting and recombination. A 3 dB coupler, which evenly divides an input signal into two output paths with equal amplitude and a 90° or 180° phase difference, can be realized using structure like branch-line couplers. For reflecting mirrors used in configurations such as the MI, physical metal-backed terminations or open-circuit stubs can serve as reflective elements in planar

circuits, while metallic walls or waveguide shorting plates are common in waveguide-based designs. The choice of implementation affects the insertion loss, phase stability, and reflection characteristics of the system, and must be optimized based on the frequency range, sensor sensitivity requirements, and integration with the sensing medium.

Microstrip hybrid couplers offer several advantages over other realizations, such as waveguide or coaxial structures, making them particularly suitable for compact and integrated microwave sensing systems. One of their main benefits is the ease of fabrication using standard printed circuit board (PCB) technology, which significantly reduces manufacturing cost and complexity. Unlike bulky waveguide couplers, microstrip designs are lightweight, planar, and easily integrated with other components such as resonators, antennas, and sensing elements on the same substrate. They also provide sufficient performance in terms of amplitude and phase balance for many practical applications, while maintaining a relatively small footprint.

3.3 Design of a Microstrip Line

The Characteristic Impedance of Microstrip Line consists of width (w), thickness (t), the distance between the line & ground plane (h) and the dielectric constant (ε_r) of the material illustrated from Figure 3-4.

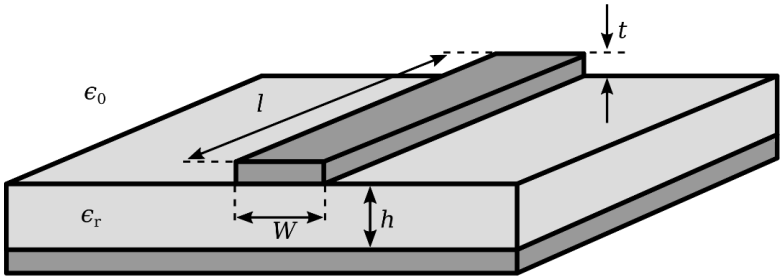

Figure 3-4 Microstrip transmission line structure and design parameters (https://en.m.wikipedia.org/wiki/File:Microstrip_scheme.svg).

The Effective Dielectric Constant $\varepsilon_{r,e}$ is expected to be greater than the dielectric constant of air ($\varepsilon_r = 1$) and less than that of the dielectric substrate. Also, $\frac{W}{h} \geq 1$

$$\varepsilon_{r,e} = \frac{\varepsilon_{r+1}}{2} + \frac{\varepsilon_r - 1}{2} \frac{1}{\sqrt{1 + 12\,{}^{h}/_{W}}} \tag{3.1}$$

Accurate expressions for wavelength λ_g, phase propagation constant β, and phase velocity v_p are obtained respectively:

$$\lambda_g = \frac{2\pi}{\beta} = \frac{\lambda_0}{\sqrt{\varepsilon_{r,e}}} \tag{3.2}$$

$$v_p = \frac{c_0}{\sqrt{\varepsilon_{r,e}}} \tag{3.3}$$

$$\beta = \beta_0 \sqrt{\varepsilon_{r,e}} \tag{3.4}$$

Characteristic impedance Z_0 of microstrip is also a function of the ratio of the height to the width W/H (and ratio of width to height H/W) of the transmission line, and has separate solutions depending on the value of W/H. According to Bahl and Trivedi [34], the characteristic impedance Z_0 of microstrip is calculated by:

$$Z_0 = \frac{120\pi}{\sqrt{\varepsilon_{r,e}} \times \left[\frac{W}{h} + 1.393 + \frac{2}{3}\ln\left(\frac{W}{h} + 1.444\right)\right]} \tag{3.5}$$

3.4 Coupler configuration

A passive microwave component which is known as coupler is engineered to distribute power, sample signals, or combine multiple signals effectively in RF and microwave systems. Common configurations include waveguide, microstrip, strip line, and coaxial couplers, each optimized for specific applications and frequency ranges. Functionally, couplers can be bidirectional, allowing signal sampling in both directions, or directional, which selectively couples power in one direction to minimize interference and enhance performance. Scattering matrix of a 4-port Network contains 16 elements which each element describe its performance and S-matrix should be symmetric and unitary. A 4-port network can be lossless, reciprocal and matched at all ports. So, the form of scattering matrix has the following form:

$$[S] = \begin{bmatrix} 0 & S_{12} & S_{13} & S_{14} \\ S_{21} & 0 & S_{23} & S_{24} \\ S_{13} & S_{23} & 0 & S_{34} \\ S_{14} & S_{24} & S_{34} & 0 \end{bmatrix} \quad (3.6)$$

3.4.1 Directional Coupler

A directional coupler is demonstrated in Figure 3-5 is a passive four-port microwave device designed to sample a small portion of an input signal while allowing most of the power to flow through the main transmission path. Key performance metrics, such as coupling factor, directivity, insertion loss, and return loss, determine its efficiency in handling signals.

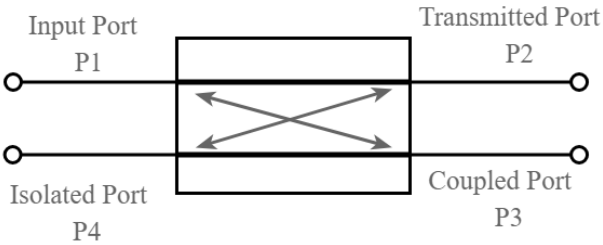

Figure 3-5 Directional Coupler [34].

The device exhibits reciprocal behaviour because, any port can act as an input, and the device will operate in the same manner (even though they use different output ports)[34].

The extracted equations from (3.6) are:

$$S_{13}^* S_{23} + S_{14} S_{24}^* = 0 \quad (3.7)$$

$$S_{14}^* S_{13} + S_{24}^* S_{23} = 0 \quad (3.8)$$

$$S_{14}^* (|S_{13}|^2 - |S_{13}|^2) = 0 \quad (3.9)$$

$$S_{12}^* S_{23} + S_{14} S_{34}^* = 0 \quad (3.10)$$

$$S_{14}^{*}S_{12} + S_{34}^{*}S_{23} = 0 \tag{3.11}$$

$$S_{23}(|S_{12}|^2 - |S_{34}|^2) = 0 \tag{3.12}$$

$$|S_{12}|^2 + |S_{13}|^2 = 1 \tag{3.13a}$$

$$|S_{12}|^2 + |S_{24}|^2 = 1 \tag{3.13b}$$

$$|S_{13}|^2 + |S_{34}|^2 = 1 \tag{3.13c}$$

$$|S_{24}|^2 + |S_{34}|^2 = 1 \tag{3.13d}$$

To satisfy the unitary condition from the equations above, both quantities can be expressed as $|S_{13}| = |S_{24}|$ and $|S_{12}| = |S_{34}|$, resulted in four-ports network configuration. By considering $S_{12} = S_{34} = \alpha$, $S_{13} = \beta e^{j\theta}$ and $S_{24} = \beta e^{j\varphi}$ where α and β are real and θ, φ are phase constant. So, the new form of the matrix for standard directional coupler is:

$$[S] = \begin{bmatrix} 0 & \alpha & \beta e^{j\theta} & 0 \\ \alpha & 0 & 0 & \beta e^{j\theta} \\ \beta e^{j\theta} & 0 & 0 & \alpha \\ 0 & \beta e^{j\theta} & \alpha & 0 \end{bmatrix} \tag{3.14}$$

A Symmetric Coupler is characterized by $\theta = \varphi = \pi/2$. The phases of the terms having amplitude β are chosen equal. The scattering matrix of the directional four ports coupler takes the following form:

$$[S] = \begin{bmatrix} 0 & \alpha & j\beta & 0 \\ \alpha & 0 & 0 & j\beta \\ j\beta & 0 & 0 & \alpha \\ 0 & j\beta & \alpha & 0 \end{bmatrix} \tag{3.15}$$

Hybrid couplers are a special type of directional couplers designed to split an input signal evenly between two output ports. This means that each output receives half

the power, which corresponds to a 3 dB coupling factor. Mathematically, this is expressed as:

$$\alpha = \beta = \frac{1}{\sqrt{2}} \tag{3.16}$$

3.4.2 Branch Line Hybrid Coupler

Quadrature Hybrid Coupler is a type of 4-port 3dB coupler with 90° phase shift between through and coupled port. Quadrature Hybrid is also well known as Branch-Line Hybrid Coupler (BLHC).

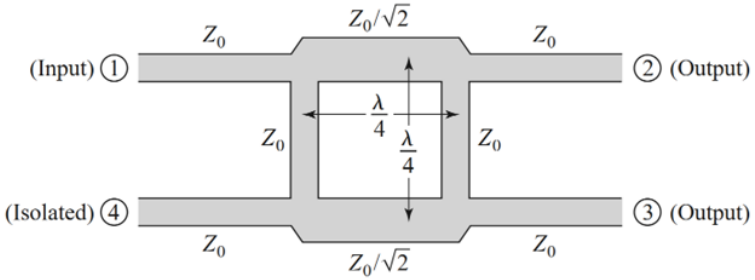

Figure 3-6 Geometry of a Branch-Line Coupler [34].

$$[S] = \frac{-1}{\sqrt{2}}\begin{bmatrix} 0 & j & 1 & 0 \\ j & 0 & 0 & 1 \\ 1 & 0 & 0 & j \\ 0 & 1 & j & 0 \end{bmatrix} \tag{3.17}$$

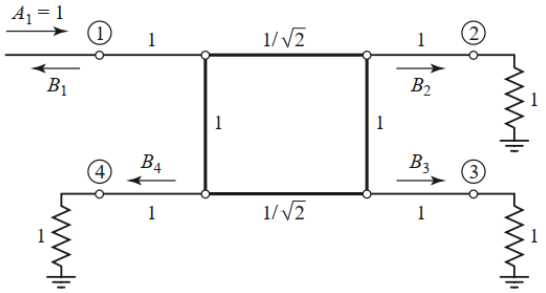

Figure 3-7 Circuit of the branch-line hybrid coupler in normalized form [34].

Considering Figure 3-6, the schematic circuit of the BLHC is drawn and shown in Figure 3-7, each line represents a transmission line with indicated characteristic impedance normalized to Z_0. The common ground return for each transmission line is not shown. We assume that a wave of unit amplitude A_1=1 is incident at port 1. Because of the symmetry or antisymmetric of the excitation, the four-port network can be decomposed into a set of two decoupled two-port networks:

Even mode(a):

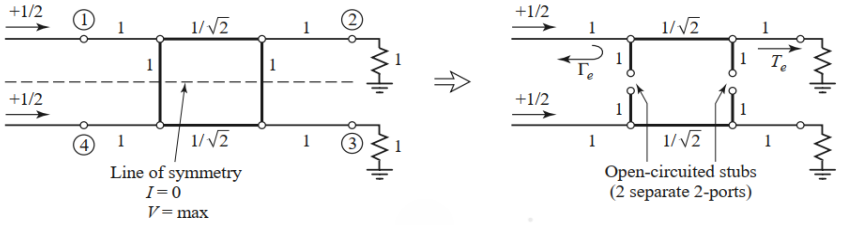

Odd mode(b):

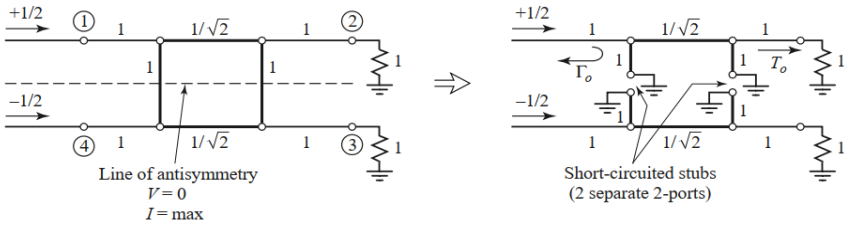

Figure 3-8 Decomposition of the branch-line coupler into even- and odd-mode excitations. a) Even mode, b) Odd mode [34].

Amplitudes of the emerging wave at each port of the branch-line hybrid can be expressed as:

$$B_1 = \frac{1}{2}\Gamma_e + \frac{1}{2}\Gamma_0 \tag{3.18a}$$

$$B_2 = \frac{1}{2}\mathrm{T}_e + \frac{1}{2}\mathrm{T}_0 \tag{3.18b}$$

$$B_3 = \frac{1}{2}T_e - \frac{1}{2}T_0 \tag{3.18c}$$

$$B_4 = \frac{1}{2}\Gamma_e - \frac{1}{2}\Gamma_0 \tag{3.18d}$$

The best way to calculate Γ_e and T_e for the even-mode two-port circuit by multiplying the *ABCD* matrices of each cascade component in that circuit can be written as below:

$$\begin{bmatrix} A & B \\ C & D \end{bmatrix}_e = \underbrace{\begin{bmatrix} 1 & 0 \\ j & 1 \end{bmatrix}}_{\substack{\text{Shunt} \\ Y = j}} \underbrace{\begin{bmatrix} 0 & j/\sqrt{2} \\ j\sqrt{2} & 0 \end{bmatrix}}_{\substack{\lambda/4 \\ \text{Transmission} \\ \text{line}}} \underbrace{\begin{bmatrix} 1 & 0 \\ j & 1 \end{bmatrix}}_{\substack{\text{Shunt} \\ Y = J}} = \frac{1}{\sqrt{2}} \begin{bmatrix} -1 & j \\ j & -1 \end{bmatrix} \tag{3.19}$$

$$\Gamma_e = \frac{A + B - C - D}{A + B + C + D} = \frac{(-1 + j - j + 1)/\sqrt{2}}{(-1 + j + j - 1)/\sqrt{2}} = 0 \tag{3.20a}$$

$$\mathrm{T}_e = \frac{2}{A+B+C+D} = \frac{2}{(-1+j+j-1)/\sqrt{2}} = \frac{-1}{\sqrt{2}}(1+j) \qquad (3.20b)$$

Similarly, for the odd mode calculation obtained as the following:

$$\begin{bmatrix} A & B \\ C & D \end{bmatrix}_o = \frac{1}{\sqrt{2}}\begin{bmatrix} 1 & j \\ j & 1 \end{bmatrix} \qquad (3.21)$$

which gives the reflection and transmission coefficients as:

$$\Gamma_o = 0 \qquad (3.22a)$$

$$\mathrm{T}_o = \frac{1}{\sqrt{2}}(1-j) \qquad (3.22b)$$

Using (7.20) and (3.22) in (3.18) gives the following results:

$B_1 = 0$ (port 1 is matched) (3.23a)

$B_2 = -\frac{j}{\sqrt{2}}$ (half-power, -90◦ phase shift from port 1 to 2) (3.23b)

$B_3 = -\frac{1}{\sqrt{2}}$ (half-power, -180◦ phase shift from port 1 to *3)* (3.23c)

$B_4 = 0$ *(no power to port 4)* (3.23d)

Each Equation in (3.23) has a meaning. (3.23a) shows that no reflected power at input port (matched port), (3.23b) shows half power amplitude of input power with -90◦ phase difference between input and through port, (3.23c) shows half power amplitude of input power with -180◦ phase difference between input and coupled port so the phase shift between through and coupled port (output ports) is 90◦. (3.23d) shows no power is delivered to isolation port[34].

3.5 Application of BLHC and Microwave Components in Distance Measurement with Interferometry

A microwave interferometer implementation using a 3dB coupler (BLHC) to split/combine signals with 90° phase shift, microstrip lines to direct microwaves

along reference and measurement paths, also reflecting mirrors to conclude each arm. Path-length difference ($2\Delta dx$) from mirror displacement induces a phase shift ($\Delta\varphi$) in the measurement signal. Recombination in the BLHC creates interference.

3.5.1 Purpose of Interferometry in MW Sensors

Microwave interferometry is a vital tool in distance sensing, providing high-precision, non-contact measurements over long distances, even in environments where optical methods may falter. Additionally, microwave-based systems are often more cost-effective compared to optical sensing techniques, making them a practical choice for various applications. Unlike optical techniques, microwaves can penetrate obstacles like fog, dust, and certain materials, making them highly effective for applications such as radar, remote sensing, and structural health monitoring. By analyzing phase shifts between transmitted and reflected microwave signals, this method achieves sub-wavelength resolution for accurate displacement and distance measurements. Furthermore, this technique leverages the conversion of phase changes into amplitude variations using BLHC, providing a robust and precise way to measure distance.

3.5.2 Purpose for utilization of BLHC in Interferometry

These patterns enable highly accurate measurements of optical paths, distances, and material properties. In this adapted Michelson interferometer, a branched-line hybrid coupler is used instead of traditional beam splitters and mirrors. It divides the input wave into two paths, which are reflected, phase-shifted, and then recombined to generate interference. Since directly measuring phase variations can be challenging, converting these phase changes into measurable signals provides a more effective and precise method for analysis. Additionally, using a branched-line hybrid coupler in a Michelson interferometer offers several advantages. It enables a compact and efficient design, making the system more space-saving and easier to integrate. The coupler ensures high precision in splitting and recombining signals, which is critical for accurate measurements.

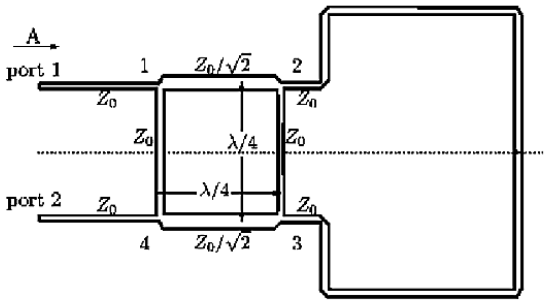

Figure 3-9 A Branch-Line Hybrid Coupler with Connected Output Ports.

An input signal with amplitude A shown in Figure 3-9, is incident on port 1 of the branch-line coupler. The coupler evenly splits this input signal between port 2 and port 3 with a 90° phase shift between the outputs.
The wave entering port 2 of the coupler has a phase of $-2\beta(L)$, while the wave entering port 3 has a phase of $-2\beta(L)$. This happens because of the outputs of the coupler are connected, making the microstrip line longer. The signal travels in one direction and then returns, so the total phase shift should be $(2\beta \times L)$.

$$\begin{bmatrix} B_1 \\ B_2 \\ B_3 \\ B_4 \end{bmatrix} = \frac{-1}{\sqrt{2}} \begin{bmatrix} 0 & j & 1 & 0 \\ j & 0 & 0 & 1 \\ 1 & 0 & 0 & j \\ 0 & 1 & j & 0 \end{bmatrix} \times \begin{bmatrix} 0 \\ \frac{A}{\sqrt{2}} e^{-j(2\beta(L)+90)} \\ \frac{A}{\sqrt{2}} e^{-j(2\beta(L)+180)} \\ 0 \end{bmatrix} \tag{3.24}$$

The reflected waves at ports 1 and 4 of the coupler come from (3.24) as below:

$$B_1 = \frac{-1}{\sqrt{2}} \times \frac{A}{\sqrt{2}} \left[j \times e^{-j(2\beta(L)+90)} + 1 \times e^{-j(2\beta(L)+180)} \right] \tag{3.25a}$$

$$B_4 = \frac{-1}{\sqrt{2}} \times \frac{A}{\sqrt{2}} \left[1 \times e^{-j(2\beta(L)+90)} + j \times e^{-j(2\beta(L)+180)} \right] \tag{3.25b}$$

$$\begin{bmatrix} B_1 \\ B_2 \\ B_3 \\ B_4 \end{bmatrix} = A \times \begin{bmatrix} \sin(2\beta dx)\, e^{-j(2\beta(L)+90)} \\ 0 \\ 0 \\ \cos(2\beta dx)\, e^{-j(2\beta(L)+270)} \end{bmatrix} \tag{3.26}$$

3.5.2.1 A Branch-Line Coupler with a Grounded Port Loaded:

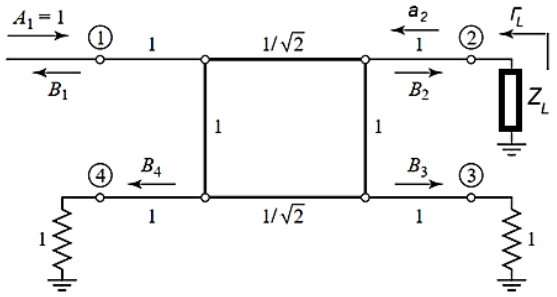

Figure 3-10 A Scheme of a BLHC with a Single Port Loaded.

The relationship between incident and reflected waves can be expressed using the branch-line coupler's S-matrix to write new S-matrix by substituting the port 2 (loaded) coefficient as follows:

$$\begin{bmatrix} b_1 \\ b_4 \end{bmatrix} = \begin{bmatrix} S_{11}{}' & S_{14}{}' \\ S_{44}{}' & S_{41}{}' \end{bmatrix} \begin{bmatrix} a_1 \\ a_4 \end{bmatrix} \tag{3.27}$$

According to Figure 3-10, the following steps are considered $a_1 = A$ (input signal), $a_2 = \Gamma b_2$ (Loaded with Mismatch) and $a_3 = a_4 = 0$ (Matched); Also, from load equation, mismatch in reflection can be extracted as below:

$$Z_L = R_L + jX_L \tag{3.28}$$

$$\Gamma = |\Gamma_L| e^{-j\varphi_\Gamma} \tag{3.29}$$

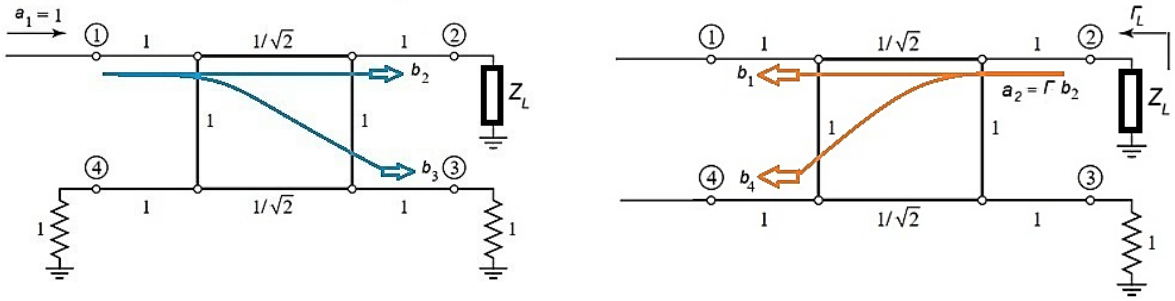

(a) (b)

Figure 3-11 a) Transmitted and b) Reflected ways of a Single Port Loaded of a BLHC scheme.

According to Figure 3-11(a), the input wave a_1 transmits to ports 2 and 3, while there is no power coupled to the isolated port 4. As shown in Figure 3-11(b), port 3 remains matched so the reflected power is zero. Since the port 2 is connected to load (Z_L), the reflected wave b_2 combines with reflection coefficient Γ_L with phase angle of φ_Γ ,which came from impedance mismatch in port 2, transmitted to ports 1 and 4.

$$b_1 = S_{11}a_1 + S_{12}a_2 + S_{13}a_3 + S_{14}a_4 \quad (3.30a)$$
$$b_2 = S_{21}a_1 + S_{22}a_2 + S_{23}a_3 + S_{24}a_4 \quad (3.30b)$$
$$b_3 = S_{31}a_1 + S_{32}a_2 + S_{33}a_3 + S_{34}a_4 \quad (3.30c)$$
$$b_4 = S_{41}a_1 + S_{42}a_2 + S_{43}a_3 + S_{44}a_4 \quad (3.30d)$$

By using (3.29) in (3.30), the reflected waves are calculated as:

$$b_2 = S_{21}a_1 + S_{22}\Gamma b_2 + S_{23}a_3 + S_{24}a_4 \quad (3.31)$$

$$b_2 = \frac{1}{(1 - \Gamma S_{22})}(S_{21}a_1 + S_{23}a_3 + S_{24}a_4) \quad (3.32)$$

$$b_1 = S_{11}a_1 + S_{12}\Gamma\left[\frac{1}{(1 - \Gamma S_{22})}(S_{21}a_1 + S_{23}a_3 + S_{24}a_4)\right] + S_{13}a_3 + S_{14}a_4 \quad (3.33)$$

$$b_1 = \left(S_{11} + \frac{S_{12}\Gamma S_{21}}{(1 - \Gamma S_{22})}\right)a_1 + \left(S_{13} + \frac{S_{12}\Gamma S_{23}}{(1 - \Gamma S_{22})}\right)a_3 + \left(S_{14} + \frac{S_{12}\Gamma S_{24}}{(1 - \Gamma S_{22})}\right)a_4 \quad (3.34)$$

$$b_3 = S_{31}a_1 + S_{32}\Gamma\left[\frac{1}{(1 - \Gamma S_{22})}(S_{21}a_1 + S_{23}a_3 + S_{24}a_4)\right] + S_{33}a_3 + S_{34}a_4 \quad (3.35)$$

$$b_3 = \left(S_{31} + \frac{S_{32}\Gamma S_{21}}{(1 - \Gamma S_{22})}\right)a_1 + \left(S_{33} + \frac{S_{32}\Gamma S_{23}}{(1 - \Gamma S_{22})}\right)a_3 + \left(S_{34} + \frac{S_{32}\Gamma S_{24}}{(1 - \Gamma S_{22})}\right)a_4 \quad (3.36)$$

$$b_4 = S_{41}a_1 + S_{42}\Gamma\left[\frac{1}{(1 - \Gamma S_{22})}(S_{21}a_1 + S_{23}a_3 + S_{24}a_4)\right] + S_{43}a_3 + S_{44}a_4 \quad (3.37)$$

$$b_4 = \left(S_{41} + \frac{S_{42}\Gamma S_{21}}{(1-\Gamma S_{22})}\right) a_1 + \left(S_{43} + \frac{S_{42}\Gamma S_{21}}{(1-\Gamma S_{22})}\right) a_3 + \left(S_{44} + \frac{S_{42}\Gamma S_{21}}{(1-\Gamma S_{22})}\right) a_4 \quad (3.38)$$

From (3.34), (3.36) and (3.38) the new reflected coefficients extracted as below:

$$S_{11}{}' = \left(S_{11} + \frac{S_{12}\Gamma S_{21}}{(1-\Gamma S_{22})}\right) \quad (3.39a)$$

$$S_{12}{}' = \left(S_{13} + \frac{S_{12}\Gamma S_{23}}{(1-\Gamma S_{22})}\right) \quad (3.39b)$$

$$S_{13}{}' = \left(S_{14} + \frac{S_{12}\Gamma S_{24}}{(1-\Gamma S_{22})}\right) \quad (3.39c)$$

$$S_{31}{}' = \left(S_{31} + \frac{S_{32}\Gamma S_{21}}{(1-\Gamma S_{22})}\right) \quad (3.39d)$$

$$S_{32}{}' = \left(S_{33} + \frac{S_{32}\Gamma S_{23}}{(1-\Gamma S_{22})}\right) \quad (3.39e)$$

$$S_{33}{}' = \left(S_{34} + \frac{S_{32}\Gamma S_{24}}{(1-\Gamma S_{22})}\right) \quad (3.39f)$$

$$S_{41}{}' = \left(S_{41} + \frac{S_{42}\Gamma S_{21}}{(1-\Gamma S_{22})}\right) \quad (3.39g)$$

$$S_{42}{}' = \left(S_{43} + \frac{S_{42}\Gamma S_{23}}{(1-\Gamma S_{22})}\right) \quad (3.39h)$$

$$S_{43}{}' = \left(S_{44} + \frac{S_{42}\Gamma S_{24}}{(1-\Gamma S_{22})}\right) \quad (3.39i)$$

Finaly, with substituting S-parameters of BLHC in the (3.39) the transfer matrix can be written:

$$b_1 = \left(S_{11} + \frac{S_{12}\Gamma S_{21}}{(1-\Gamma S_{22})}\right) = \left(0 + \frac{-\frac{j}{\sqrt{2}} \times \Gamma \times -\frac{j}{\sqrt{2}}}{(1)}\right) A = -\frac{1}{2}\Gamma A = \frac{1}{2} A|\Gamma_L| e^{-j(\varphi_\Gamma - 180)} \quad (3.40a)$$

$$b_3 = \left(S_{31} + \frac{S_{32}\Gamma S_{21}}{(1-\Gamma S_{22})}\right) a_1 = \left(-\frac{1}{\sqrt{2}} + \frac{0}{(1)}\right) A = -\frac{1}{\sqrt{2}} A = \frac{1}{\sqrt{2}} A e^{-j(180)} \quad (3.40b)$$

$$b_4 = \left(S_{41} + \frac{S_{42}\Gamma S_{21}}{(1-\Gamma S_{22})}\right) a_1 = \left(0 + \frac{-\frac{1}{\sqrt{2}} \times \Gamma \times -\frac{j}{\sqrt{2}}}{(1)}\right) A = \frac{1}{2} A\Gamma j = \frac{1}{2} A|\Gamma_L| e^{-j(\varphi_\Gamma - 270)} \quad (3.40c)$$

$$\begin{bmatrix} b_1 \\ b_3 \\ b_4 \end{bmatrix} = A \begin{bmatrix} \frac{1}{2}|\Gamma_L| e^{-j(\varphi_\Gamma - 180)} \\ \frac{1}{\sqrt{2}} e^{-j(180)} \\ \frac{1}{2}|\Gamma_L| e^{-j(\varphi_\Gamma - 270)} \end{bmatrix} \quad (3.41)$$

This calculation in (3.41), clearly shows that the difference in angles, $\measuredangle S_{44} - \measuredangle S_{11}$, remains unaffected by variations in $\Gamma \angle \varphi_L$.

3.5.2.2 A Branch-Line Coupler with two Grounded ports loaded:

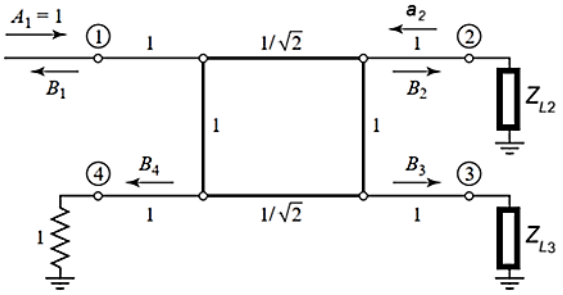

Figure 3-12 A Scheme of a BLHC with both output Ports Loaded.

The relationship between incident and reflected waves can be expressed using the branch-line coupler's S-matrix to write new S-matrix by substituting ports 2 and 3 (loaded ports) coefficient as follows:

$$\begin{bmatrix} b_1 \\ b_4 \end{bmatrix} = \begin{bmatrix} S_{11}{}' & S_{14}{}' \\ S_{44}{}' & S_{41}{}' \end{bmatrix} \begin{bmatrix} a_1 \\ a_4 \end{bmatrix} \tag{3.42}$$

According to Figure 3-12, the following steps are considered $a_1 = A$ (input signal), $a_2 = \Gamma_{L2} b_2$, $a_3 = \Gamma_{L3} b_3$ (Loaded with Mismatch) and $a_4 = 0$ (Matched); Also, from load equation, mismatch in reflection can be extracted same as (3.28) and (3.29).

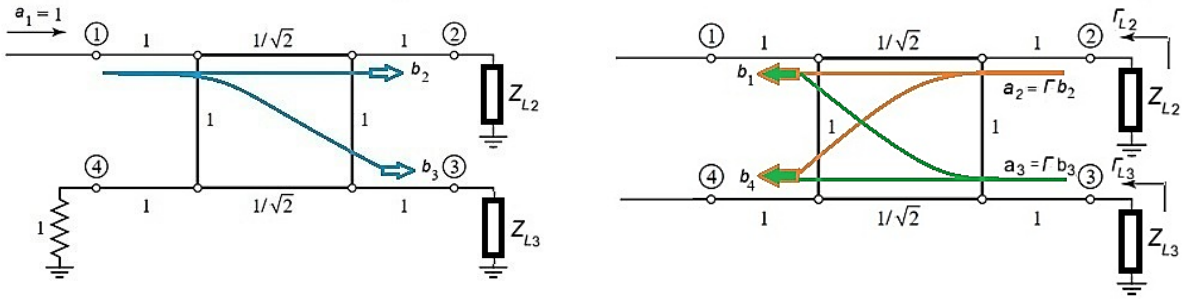

(a) (b)

Figure 3-13 a) Transmitted and b) Reflected ways of output Ports Loaded of a BLHC scheme.

According to Figure 3-13(a), the input wave a_1 transmits to ports 2 and 3, while there is no power coupled to the isolated port 4 (the reflected power is zero). Since, port 2 and 3 are connected to load (Z_L). As shown in Figure 3-13(b), the reflected wave b_2 and b_3 combine with reflection coefficient $\Gamma_{L2}\angle\varphi_{\Gamma L3}$ and $\Gamma_{L3}\angle\varphi_{\Gamma L3}$ respectively. Those came from an impedance mismatch in port 2 and 3, which transmitted to ports 1 and 4.

By substituting (3.29) in (3.30), the reflected waves can calculate as the following:

$$b_1 = S_{11}a_1 + S_{12}\Gamma_{L2}b_2 + S_{13}\Gamma_{L3}b_3 + S_{14}a_4 \tag{3.43a}$$

$$b_2 = S_{21}a_1 + S_{22}\Gamma_{L2}b_2 + S_{23}\Gamma_{L3}b_3 + S_{24}a_4 \tag{3.43b}$$

$$b_3 = S_{31}a_1 + S_{32}\Gamma_{L2}b_2 + S_{33}\Gamma_{L3}b_3 + S_{34}a_4 \tag{3.43c}$$

$$b_4 = S_{41}a_1 + S_{42}\Gamma_{L2}b_2 + S_{43}\Gamma_{L3}b_3 + S_{44}a_4 \tag{3.43d}$$

$$b_2 = \frac{1}{(1-\Gamma_{L2}S_{22})}(S_{21}a_1 + S_{23}\Gamma_{L3}b_3 + S_{24}a_4) \quad (3.44)$$

$$b_3 = \frac{1}{(1-\Gamma_{L3}S_{33})}(S_{31}a_1 + S_{32}\Gamma_{L2}b_2 + S_{34}a_4) \quad (3.45)$$

By considering b_3 and substituting b_2 from (3.43b) into (3.43c), the reflected wave(b_3) can calculate as below:

$$b_3 = S_{31}a_1 + \frac{S_{32}\Gamma_{L2}}{(1-\Gamma_{L2}S_{22})}(S_{21}a_1 + S_{23}\Gamma_{L3}b_3 + S_{24}a_4) + S_{33}\Gamma_{L3}b_3 + S_{34}a_4 \quad (3.46)$$

$$b_3 = \left[\frac{S_{31} + \frac{S_{32}\Gamma_{L2}S_{21}}{1-\Gamma_{L2}S_{22}}}{1-\Gamma_{L2}S_{22} - \frac{S_{32}\Gamma_{L2}S_{23}\Gamma_{L3}}{1-\Gamma_{L2}S_{22}}}\right]a_1 + \left[\frac{S_{34} + \frac{S_{32}\Gamma_{L2}S_{24}}{1-\Gamma_{L2}S_{22}}}{1-\Gamma_{L3}S_{33} - \frac{S_{32}\Gamma_{L2}S_{23}\Gamma_{L3}}{1-\Gamma_{L2}S_{22}}}\right]a_4 \quad (3.47)$$

By considering b_2 and substituting b_3 from (3.43c) into (3.43b), the reflected wave(b_2) can calculate as below:

$$b_2 = S_{21}a_1 + S_{22}\Gamma_{L2}b_2 + \frac{S_{23}\Gamma_{L3}}{(1-\Gamma_{L3}S_{33})}(S_{31}a_1 + S_{32}\Gamma_{L2}b_2 + S_{34}a_4) + S_{24}a_4 \quad (3.48)$$

$$b_2 = \left[\frac{S_{21} + \frac{S_{23}\Gamma_{L3}S_{31}}{1-\Gamma_{L3}S_{33}}}{1-\Gamma_{L2}S_{22} - \frac{S_{23}\Gamma_{L3}S_{32}\Gamma_{L2}}{1-\Gamma_{L3}S_{33}}}\right]a_1 + \left[\frac{S_{24} + \frac{S_{23}\Gamma_{L3}S_{34}}{1-\Gamma_{L3}S_{33}}}{1-\Gamma_{L2}S_{22} - \frac{S_{23}\Gamma_{L3}S_{32}\Gamma_{L2}}{1-\Gamma_{L3}S_{33}}}\right]a_4 \quad (3.49)$$

From substituting (3.47), (3.49) into (3.43), new reflected coefficients extracted as below:

$$S'_{11} = \frac{b_1}{a_1}\left[S_{11} + \frac{S_{12}\Gamma_{L2}S_{21} + \frac{S_{12}\Gamma_{L2}S_{23}\Gamma_{L3}S_{31}}{1-\Gamma_{L3}S_{33}}}{1-\Gamma_{L2}S_{22} - \frac{S_{23}\Gamma_{L3}S_{32}\Gamma_{L2}}{1-\Gamma_{L3}S_{33}}} + \frac{S_{13}\Gamma_{L3}S_{31} + \frac{S_{13}\Gamma_{L3}S_{32}\Gamma_{L2}S_{21}}{1-\Gamma_{L2}S_{22}}}{1-\Gamma_{L2}S_{22} - \frac{S_{32}\Gamma_{L2}S_{23}\Gamma_{L3}}{1-\Gamma_{L2}S_{22}}}\right] \quad (3.50a)$$

$$S'_{14} = \frac{b_1}{a_4}\left[S_{14} + \frac{S_{24}S_{12}\Gamma_{L2} + \frac{S_{23}\Gamma_{L3}S_{34}S_{12}\Gamma_{L2}}{1-\Gamma_{L3}S_{33}}}{1-\Gamma_{L2}S_{22} - \frac{S_{23}\Gamma_{L3}S_{32}\Gamma_{L2}}{1-\Gamma_{L3}S_{33}}} + \frac{S_{34}S_{13}\Gamma_{L3} + \frac{S_{32}\Gamma_{L2}S_{24}S_{13}\Gamma_{L3}}{1-\Gamma_{L2}S_{22}}}{1-\Gamma_{L3}S_{33} - \frac{S_{32}\Gamma_{L2}S_{23}\Gamma_{L3}}{1-\Gamma_{L2}S_{22}}}\right] \tag{3.50b}$$

$$S'_{41} = \frac{b_4}{a_1}\left[S_{41} + \frac{S_{42}\Gamma_{L2}S_{21} + \frac{S_{42}\Gamma_{L2}S_{23}\Gamma_{L3}S_{31}}{1-\Gamma_{L3}S_{33}}}{1-\Gamma_{L2}S_{22} - \frac{S_{23}\Gamma_{L3}S_{32}\Gamma_{L2}}{1-\Gamma_{L3}S_{33}}} + \frac{S_{43}\Gamma_{L3}S_{31} + \frac{S_{43}\Gamma_{L3}S_{32}\Gamma_{L2}S_{21}}{1-\Gamma_{L2}S_{22}}}{1-\Gamma_{L2}S_{22} - \frac{S_{32}\Gamma_{L2}S_{23}\Gamma_{L3}}{1-\Gamma_{L2}S_{22}}}\right] \tag{3.50c}$$

$$S'_{44} = \frac{b_4}{a_4}\left[\frac{S_{24}S_{42}\Gamma_{L2} + \frac{S_{23}\Gamma_{L3}S_{34}S_{42}\Gamma_{L2}}{1-\Gamma_{L3}S_{33}}}{1-\Gamma_{L2}S_{22} - \frac{S_{23}\Gamma_{L3}S_{32}\Gamma_{L2}}{1-\Gamma_{L3}S_{33}}} + \frac{S_{34}S_{43}\Gamma_{L3} + \frac{S_{32}\Gamma_{L2}S_{24}S_{43}\Gamma_{L3}}{1-\Gamma_{L2}S_{22}}}{1-\Gamma_{L3}S_{33} - \frac{S_{32}\Gamma_{L2}S_{23}\Gamma_{L3}}{1-\Gamma_{L2}S_{22}}}\right] \tag{3.50d}$$

Finally, with substituting S-parameters of BLHC in the (3.50) the coefficients of the transfer matrix can be written, If $|\Gamma_{L2}| = |\Gamma_{L2}| = |\Gamma|$ and if $\varphi_3 = -\varphi_2$:

$$b_1 = S'_{11}a_1 = \frac{A}{2}\left[|\Gamma_{L3}|e^{-j\varphi_3} - |\Gamma_{L2}|e^{-j\varphi_2}\right] = A|\Gamma|e^{-j90}\,sin\,\varphi_3 \tag{3.51a}$$

$$b_4 = S'_{41}a_1 = \frac{A}{2}j\left[|\Gamma_{L2}|e^{-j\varphi_2} + |\Gamma_{L3}|e^{-j\varphi_3}\right] = A|\Gamma|e^{-j270}\,cos\,\varphi_3 \tag{3.51b}$$

3.5.3 Split Ring Resonators (SRR)

A Split Ring Resonator (SRR) consists of two metal rings placed one inside the other, with small gaps between them. These rings are typically etched onto a non-

conductive material. When an external EM field interacts with the rings, it creates currents within them, leading to a powerful magnetic resonance. By tweaking the size of the rings or the width of the gaps, the resonance frequency can be finely adjusted. This flexibility makes SRRs incredibly useful for a wide range of applications.

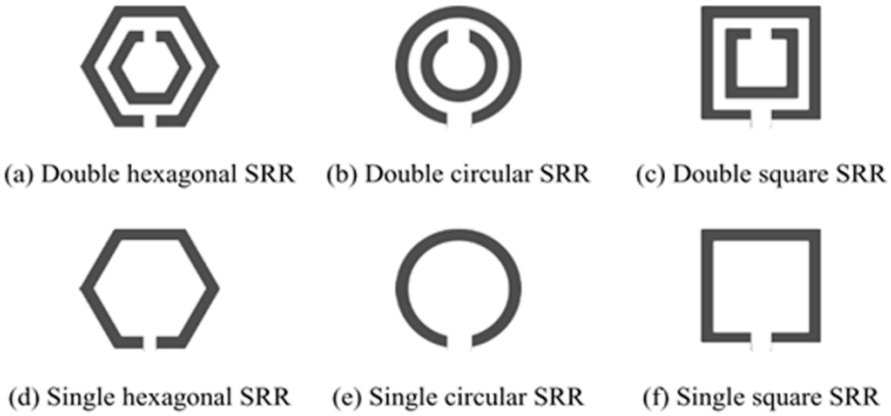

Figure 3-14 Various shapes of SRR structure rings [35].

3.5.3.1 Mathematical Modelling of SRRs

The dimensions of the single split-ring structure include inner radius (R), height (h), thickness (w), and gap width (g). The equivalent circuit of the single split resonator consists of inductance (L) and capacitance (C). The resonance frequency of an SRR can be expressed by using equivalent circuit models, as:

$$f_r = \frac{1}{2\pi\sqrt{LC_{total}}} \tag{3.52}$$

Upon observing Figure 3-14, various split-ring shapes can be seen, which significantly influence the properties of the SRR. Circular, square, and hexagonal SRRs show different frequency shifts even with similar sizes. The shape also impacts the equivalent inductance (L) and capacitance (C), which depend on the ring dimensions. A variation of L and C can be made by modifying the SRR structure.

For a single split-ring resonator, the inductance is dependent on the constructional parameters and is expressed as:

$$L = \mu_0(R + \frac{w}{2})(\ln\frac{8(R + {}^{w}/_{2})}{h + w} - 0.5) \quad (3.53)$$

The gap capacitance and surface capacitance can be given by the following equations, respectively:

$$C_{gap} = \varepsilon_0[\frac{wh}{g} + \frac{2\pi h}{\ln\left(\frac{2.4h}{w}\right)}] \quad (3.54)$$

$$C_{surface} = \frac{2\varepsilon_0 h}{\pi}(\ln\,(\frac{4R}{g})) \quad (3.55)$$

The total capacitance of the resonator is equal to:

$$C_{total} = C_{gap} + C_{surface} \quad (3.56)$$

The resonance frequency of a single SRR can be finely tuned by adjusting its size (length, width, radius, and height), from the above equations. This makes SRRs super useful in filters, oscillators, and mixers. They're especially handy in RF circuits, like demodulators and synthesizers, where precise frequency control is needed.

Chapter 4:

Results and Discussion

This chapter covers full-wave simulation for all the subjects as below and experimental results for various BLHC, SRR and interferometric sensors.

4.1 BLHC design

The BLHCs are analyzed using tools like MATLAB shows in Figure 4-1 and ADS to find proximate width and length sizes, CST, and HFSS, focusing on full-wave simulations of S-parameters, phase difference, and isolation. The coupler was designed to operate at 2.5GHz, with dimensions optimized for minimal insertion loss and maximum isolation.

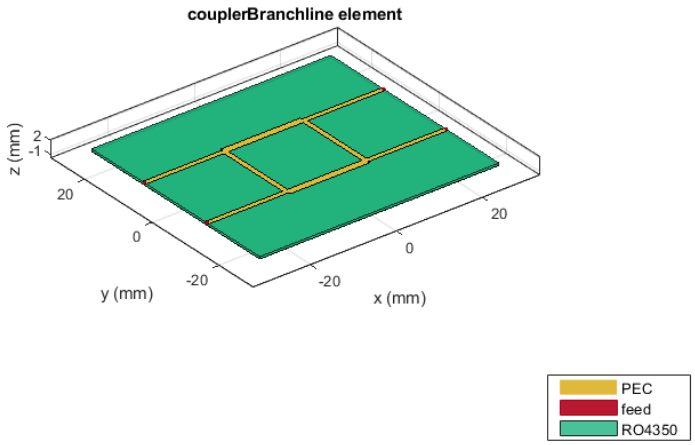

Figure 4-1 3D Model of the BLHC.

Figure 4-2 illustrates simulation setup for BLHC on ADS. The s-parameter solver selected for simulation in the 2 – 3GHz range of frequency. The schematic is done on RO-4350B standard substrate with electrical permittivity of $\varepsilon = 3.66$, with thickness of 0.508mm. MLIN models of the microstrip line with mentioned length and width, characterizing the phase difference and impedance. MTEE models of three-way junction which matches the connected ports. Finally, the ports normalized to 50ohms are utilized for excitation.

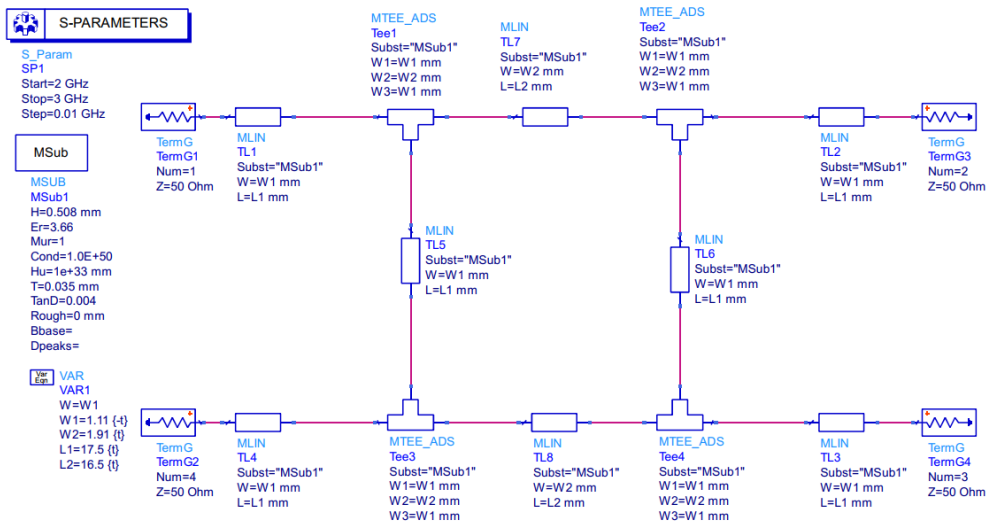

Figure 4-2 Simulation of a BLHC on ADS.

Figure 4-3 shows the scattering parameters of the BLHC illustrated in Figure 4-2. As expected, the S(1,1) and S(4,4) exhibiting the reflection coefficients imply the perfect matching (The reflection coefficient below -10dB). The equal power division can be concluded from the S(2,1) and S(3,1) with approximately 3dB loss; based on the eqn. (3.23) quadrature phase difference between port no.2 and no.3 are deduced from the phase diagram of both S(2,1) and S(3,1).

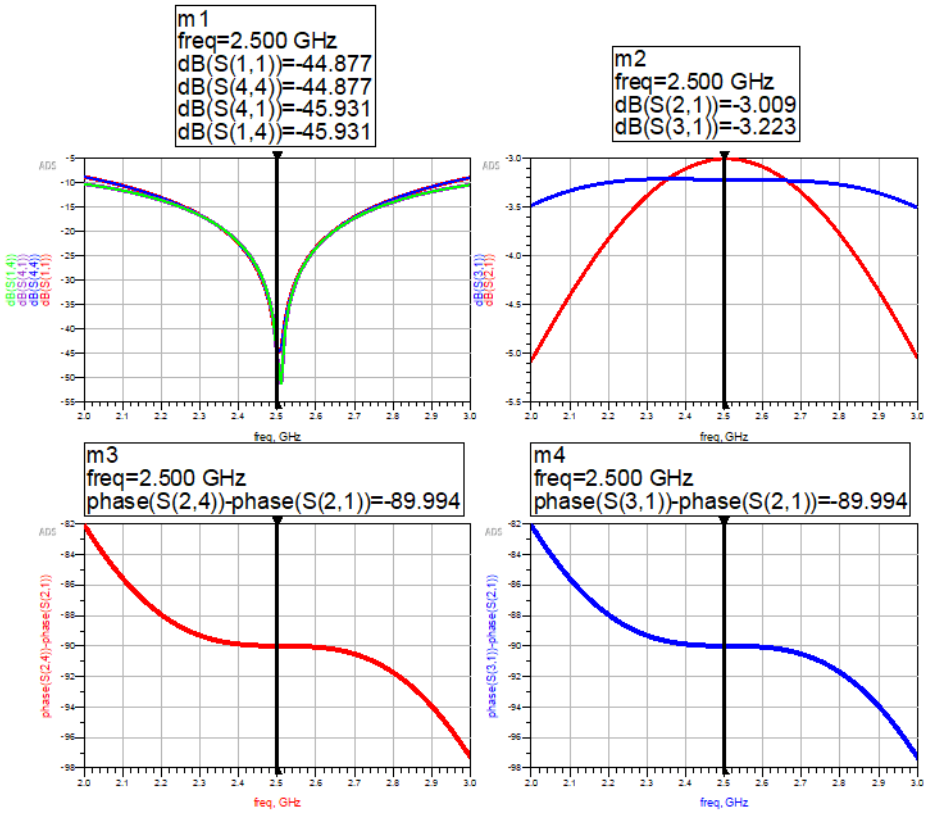

Figure 4-3 S-parameters and Phase differences Results of a BLHC Simulation designed on ADS.

The 3D model of proposed BLHC on ANSYS HFSS is demonstrated in Figure 4-4. The FEM (finite element method) solver of HFSS is utilized for accurate full-wave simulation.

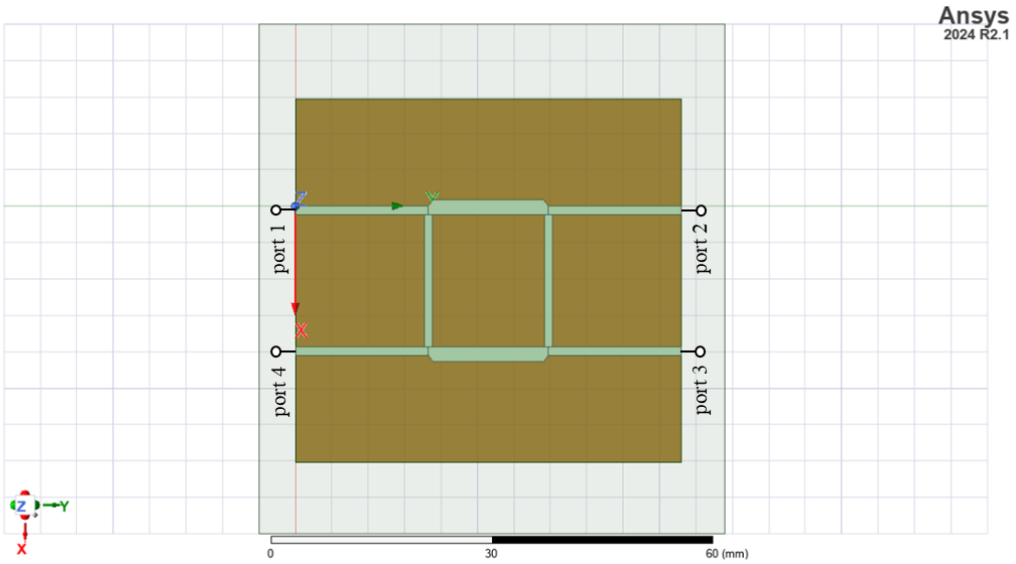

Figure 4-4 Simulation of a BLHC on Ansys HFSS.

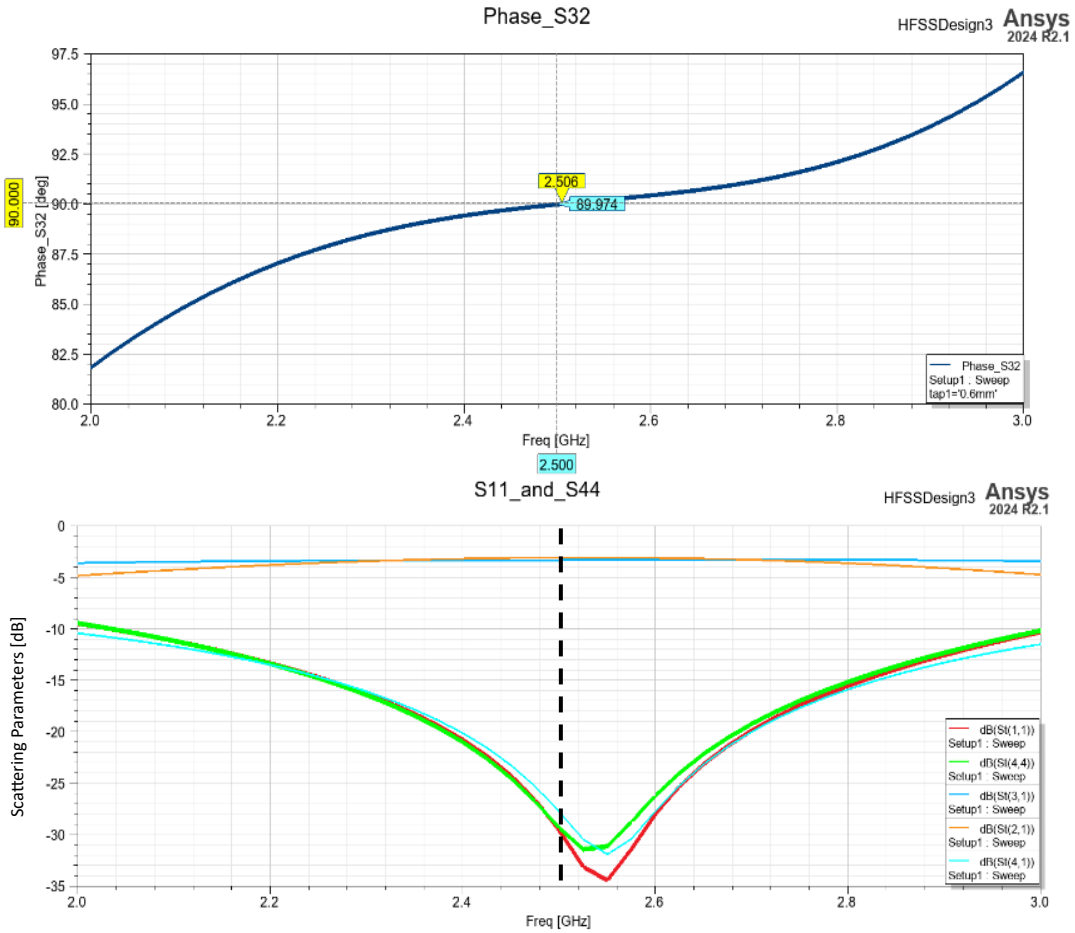

Figure 4-5 Insertion loss, Reflection coefficient loss, and Phase differences of a BLHC Designed and simulated on Ansys HFSS.

Figure 4-5 shows that the results of S-parameters obtained from HFSS are in good agreement with the results of ADS software shown in Figure 4-3; However, HFSS provides more accurate and reliable results compared to MoM method solver of ADS.

The simulated S-parameters for the BLHC in ADS, CST, and HFSS are presented in Table 4.1, showing the return loss (S11), insertion loss (S21, S31), and isolation (S41). The phase difference between the output ports is also evaluated.

Table 4-1 Simulated S-Parameters of BLHC.

Simulated S-Parameters of BLHC			
Parameter	**ADS**	**CST**	**HFSS**
S_{11}(dB)	< -40	< -30	< -30
S_{21}(dB)	< -40	< -30	< -30
S_{31}(dB)	< -40	< -30	< -30
S_{41}(dB)	< -40	< -30	< -30
$S_{31} - S_{21}$(degree)	90	90	90

Table 4-2 summarizes the size parameters of BLHC in ADS, CST, and HFSS. Exhibiting the minor details between different software.

Table 4-2 Size Parameter of BLHC.

Size Parameter of BLHC			
Parameter	**ADS (mm)**	**CST (mm)**	**HFSS (mm)**
W1	1.11	1.11	1.11
W2	1.91	1.96	1.96
L1	17.5	18.3	18.3
L2	16.5	16.5	16.5

4.2 A BLHC with Dual Grounded ports design

According to 3.4.2.2, the structure of BLHC with two grounded ports is simulated in both MATLAB and ADS software to validate the mathematical theory. The MATLAB calculation results for schematic Figure 3-10 are illustrated in Figure 4-6, exhibiting same characteristics. The MATLAB codes can be seen in Appendix (A).

As shown in Figure 4-6b, the Γ_1 and Γ_2 produce an orthogonal behavior, which validates eqn. (3-51) with 90-degree phase differences.

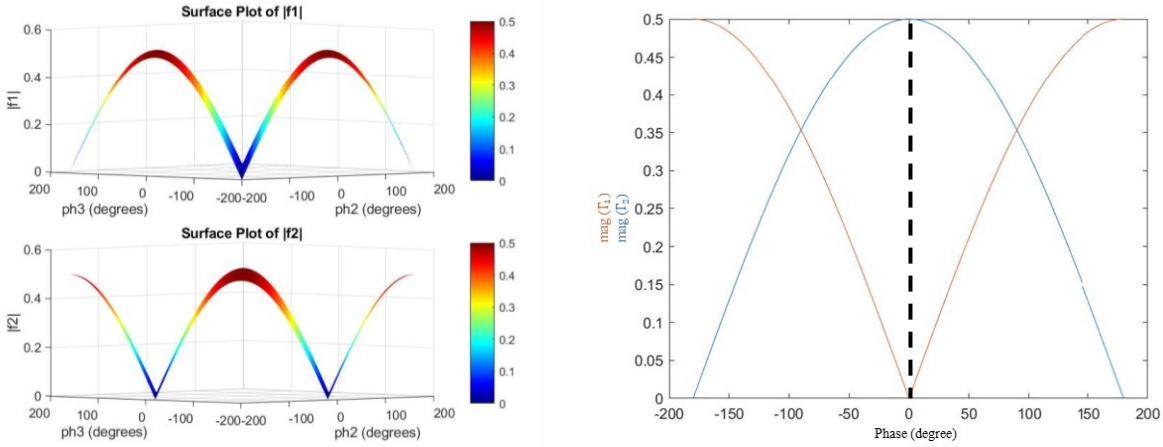

(a) (b)

Figure 4-6 MATLAB a) 3D graph, b) 2D graph of a BLHC with two grounded output ports.

The ADS schematic of the mentioned structure is demonstrated in Figure 4-7 using microstrip lines and junctions with two matched and two grounded ports.

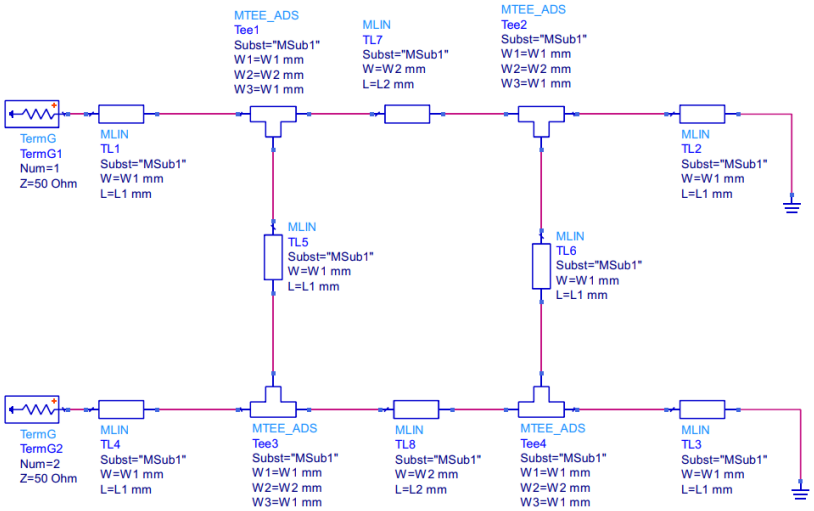

Figure 4-7 ADC schematic of a BLHC with two grounded output ports.

As expected, by examining Figure 4-8, S(2,1) of the schematic shown in Figure 4-7 tends to unity, while the S(1,1) below -50dB which illustrates the perfect matching.

The ADS simulation results presented in Figure 4-8 validate the MATLAB calculations implying the 90-degree phase difference with Γ_1 and Γ_2.

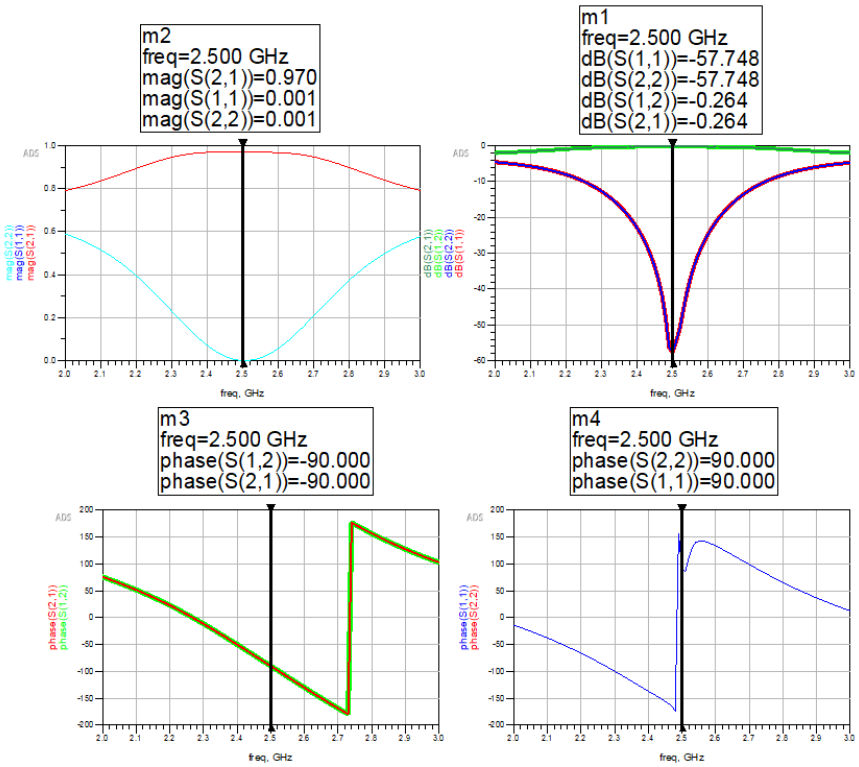

Figure 4-8 The simulation scattering parameters of a BLHC with two grounded output ports on ADS.

4.2.1 Analysis of Reflection Coefficient of a BLHC with two Grounded Ports Vs One Variable length

In this case, the length of the output microstrip line has been considered as a variable while, the other output microstrip line remained unchanged. The s-parameters for this subject evaluated in both MATLAB and ADS. L_2 is the length of the variable output and results of MATLAB simulation are illustrated in Figure 4-11; For the value of L_2 between 15-20 mm, S(2,1) reaches maximum while S(1,1) decreases its minimum quantity. S-parameters exhibit symmetrical behavior toward other values of L_2. The MATLAB codes are available in Appendix (B).

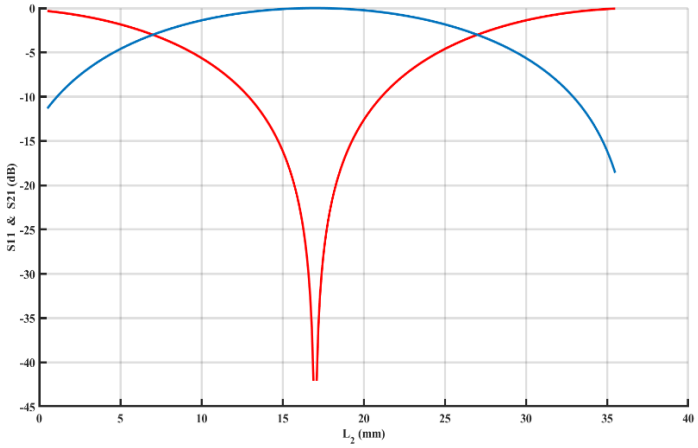

Figure 4-9 Variation of S-Parameters Versus L_2 Length on MATLAB.

Like the results obtained from MATLAB, it is obvious from Figure 4-11 for L2=17mm, S(2,1) of the schematic depicted in figure 4-10 decreases to its minimum value and illustrates symmetrical behavior in respect to mentioned point.

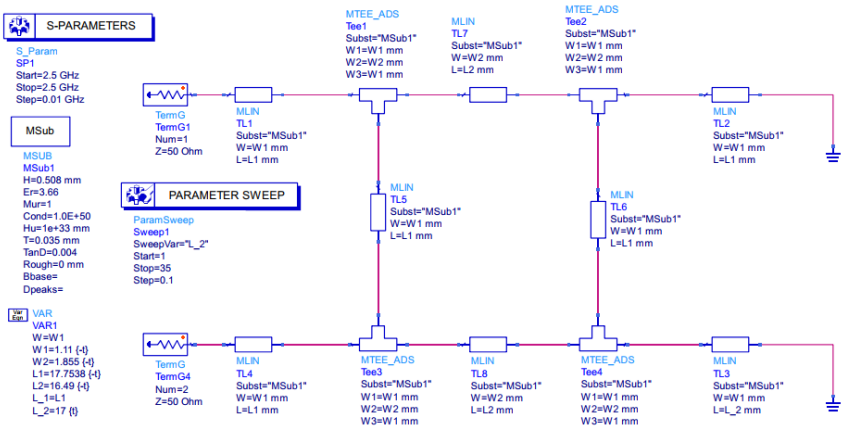

Figure 4-10 ADS Simulation of BLHC with Two Grounded Ports Vs One Variable Length L_2.

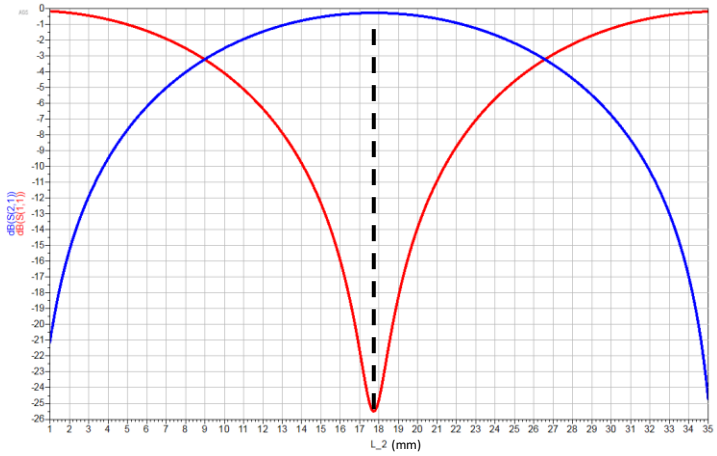

Figure 4-11 Simulated results of Reflection Coefficient and Amplitude of Transmission Coefficient, Versus Branch Length L_2 in ADS.

For higher accuracy, the structure has been modeled in Figure 4-12 as a finite length within the HFSS full-wave simulator. In this analysis, the principle of varying one of the lengths is implemented by repositioning the shorted via that connects the ground and the microstrip line L_2.

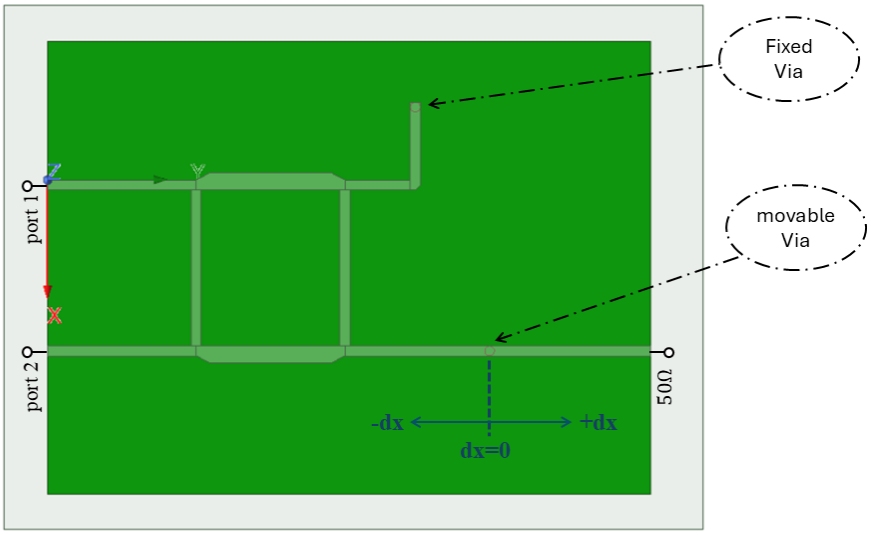

Figure 4-12 Simulation of BLHC with Two Grounded Ports by using Via on HFSS.

Figure 4-13 presents simulated results of the reflection coefficient and transmission amplitude versus via displacement (dx1 in mm). This analysis highlights the impact of via positioning on the structure's electrical characteristics, particularly reflection and transmission at 2.55 GHz, akin to the Michelson interferometric concept.

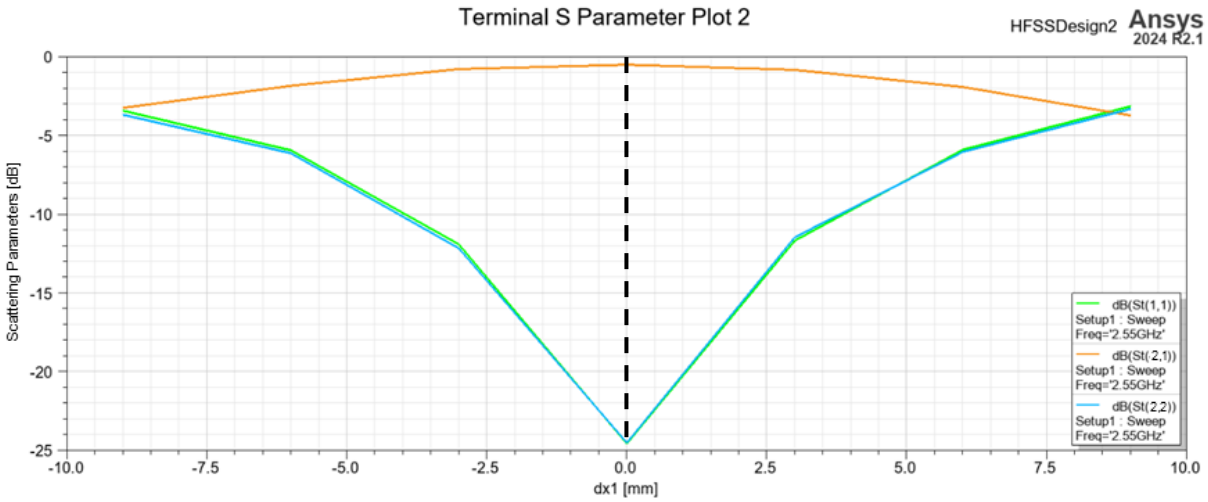

Figure 4-13 Simulated results of Reflection Coefficient and Amplitude of Transmission Coefficient, Versus Via displacement in HFSS.

4.3 SRR design and parameter extraction:

According to eqs. (3-52) – (3-56), the electrical and dimension parameters of SRR for the resonance frequency of the 2.5GHz can be derived as follow:

$$2\pi R = 4a \tag{4.1}$$

$$R = \frac{20.2}{3.1415} = 6.43mm \tag{4.2}$$

Here, a is the square side of the SRR. While the eqs. (3-52) – (3-56), are calculated for circular SRR, eqn. (4.1) is applied to equivalence the formulas for squared SRR.

$$L = 4\pi \times 10^{-7}(6.43 + \frac{1}{2})(\ln\frac{8\left(6.43 + {}^{1}/_{2}\right)}{0.508 + 1} - 0.5) = 31.26nH \tag{4.3}$$

$$C_{gap} = 8.85 \times 10^{-12}\left[\frac{0.508}{0.4} + \frac{2\pi 0.508}{\ln(1.2192)}\right] = 0.154\ pF \tag{4.4}$$

$$C_{surface} = \frac{8.9916 \times 10^{-12}}{\pi}\left(ln\ (\frac{4 \times 6.43}{0.4})\right) = 0.6874\ fF \tag{4.5}$$

$$f_r = \frac{1}{6.28 \times \sqrt{31.26 \times 10^{-9} \times 0.154 \times 10^{-12}}} \approx 2.294GHz \tag{4.6}$$

4.4 Displacement Sensor Design:

4.4.1 Microstrip line Design

A microstrip Line presented in Figure 4-14 normalized to 50ohm designed and simulated in CST.

Figure 4-14 Schematic view of the proposed Microstrip Line.

Proposed results shown in Figure 4-15 represent the perfect matching between two ports in 2.5GHz.

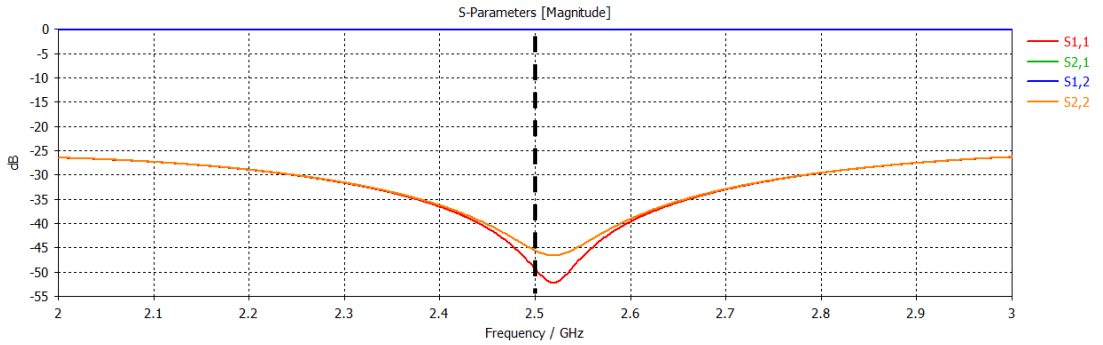

Figure 4-15 Full-wave simulation results of S-Parameters in resonance frequency.

4.4.1.1 Double SRR Structure

Investigating the possibility of location detection, the structure in Figure 4-16 with two SRR probes sweeping around the microstrip line has been introduced. The phase variation of the scattering parameters is utilized for location detection as a displacement sensor; However, phase detection using VNA is challenging, thereby, interferometric structure such as Michelson is designed to obtain scattering parameters amplitude by converting the phase variation. The reason behind

selecting this structure is the similarity to interferometric Michelson displacement sensor which will be discussed in later sections.

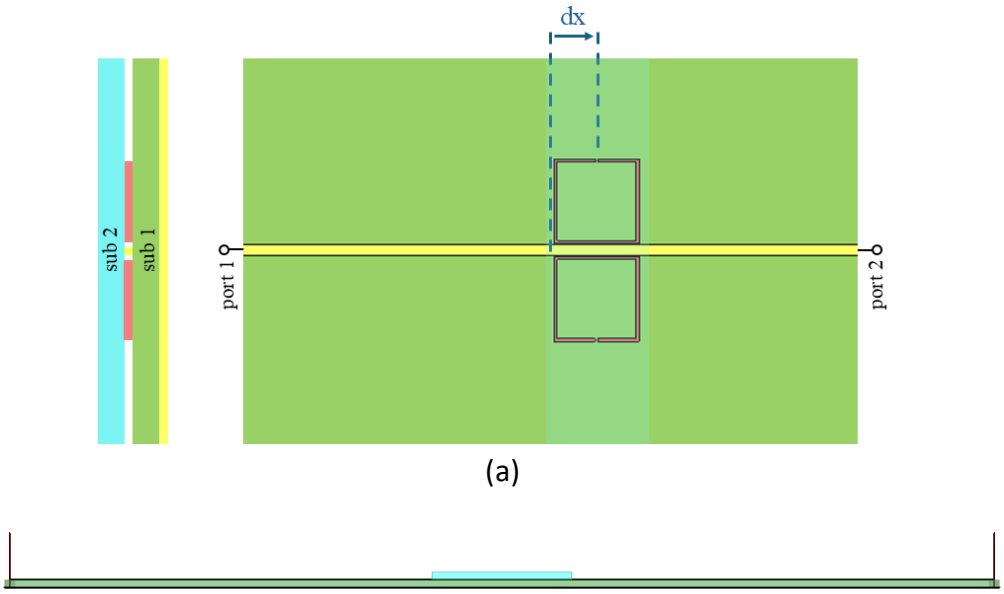

Figure 4-16 Proposed structure for displacement sensing simulated in CST.
a) Top view, b) Side view.

Figure 4-17 illustrates the magnitude of S-parameters emphasizing fixed behavior through the longitudinal sweep with resonance characteristic at the frequency of 2.5GHz; While, obviously from Figure 4-18, the phase of the S(1,1) is modified by sweeping the SRR probe. Therefore, the simulation results show that the amount of displacement can be sensed by measuring the phase of the S(1,1). Details in Figure 4-19 show the evaluation of phase variation reveals linear response with sensitivity of 11˚/mm.

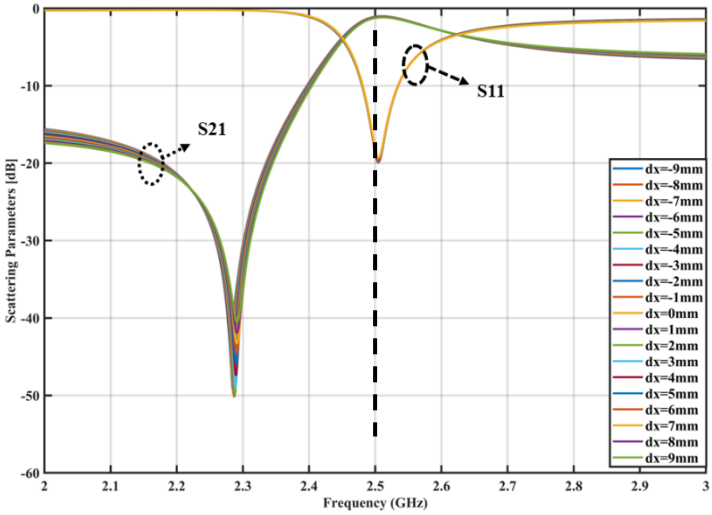

Figure 4-17 Simulated magnitude of the transmission and reflection coefficients of the proposed sensor versus frequency for different values of displacement dx.

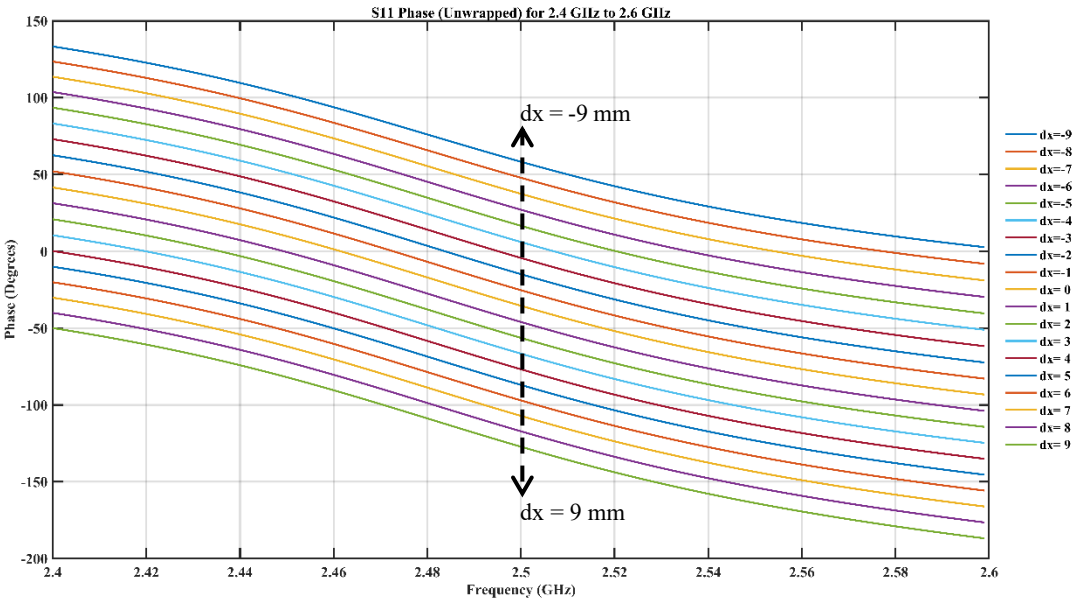

Figure 4-18 Simulated phase of the reflection coefficient for different values of displacement dx from −9 to 9 mm in steps of 1 mm.

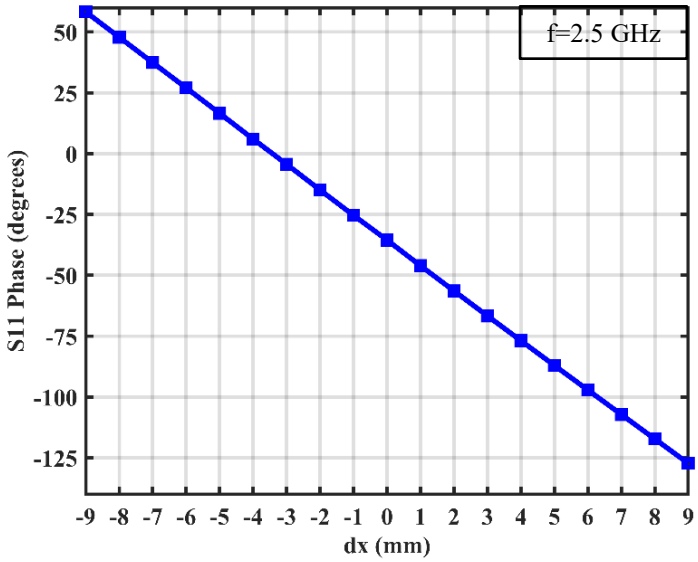

Figure 4-19 Simulated phase of the reflection coefficient in terms of displacement dx at the resonance frequency of the pair of SRRs f = 2.5 GHz.

4.4.1.2 Single SRR Structure

A new structure shown in Figure 4-20 with single SRR probe sweeping between two adjacent microstrip lines. This structure is proposed to exhibit the phase variation among the probe displacement. Nevertheless, the measurement of phase difference is more difficult than the measurement of the amplitude of a signal, hence, the Mach Zehnder interferometric displacement sensor will be discussed in the last section.

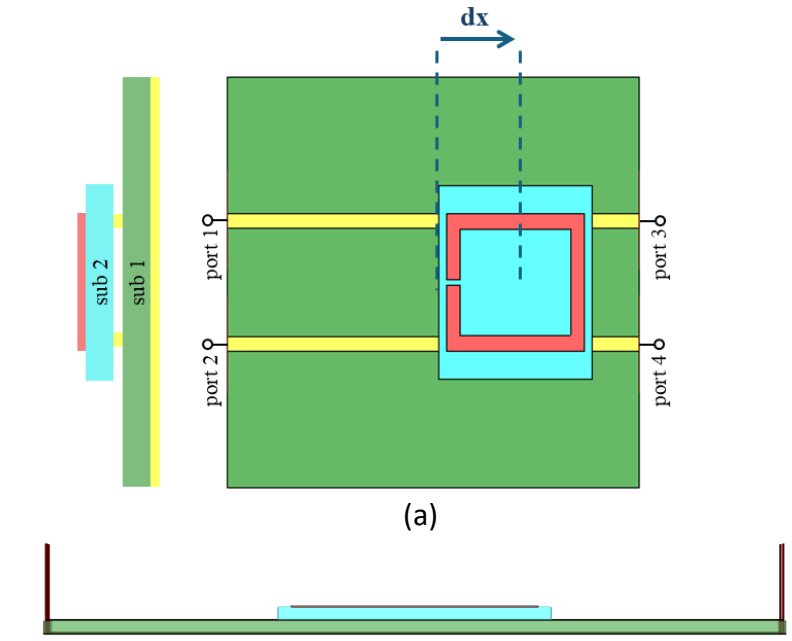

Figure 4-20 Schematic view of the proposed four ports displacement sensing. a) Top view, b) Side view.

Figure 4-21 illustrates the magnitude of reflection and transmission coefficient in the four ports network in Figure 4-20 implying steady behavior through the longitudinal sweep with resonance characteristic at the frequency of 2.5GHz; While, obviously from Figure 4-22, the phase of the reflection (S(1,1)) and transmission (S(2,1)) coefficients is changed by sweeping the SRR probe.

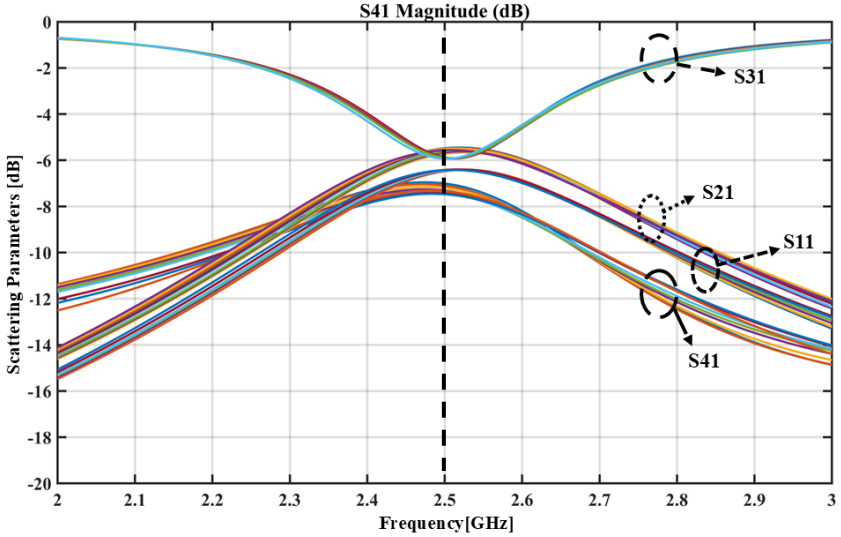

Figure 4-21 Simulated magnitude of the S-Parameters of the proposed four ports sensor versus frequency for different values of displacement dx.

Therefore, again the simulation results show that the amount of displacement can be sensed by measuring the phase of the S(1,1) and S(2,1). Further evaluation of

phase variation from Figure 4-23 reveals linear response with sensitivity of 12°/mm.

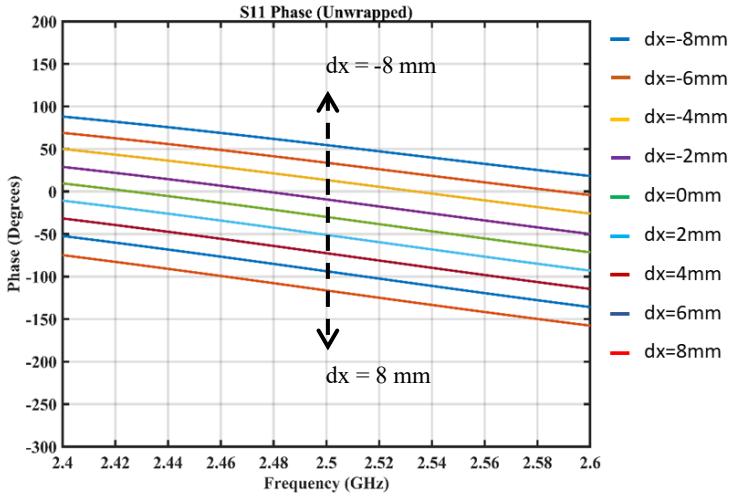

(a)

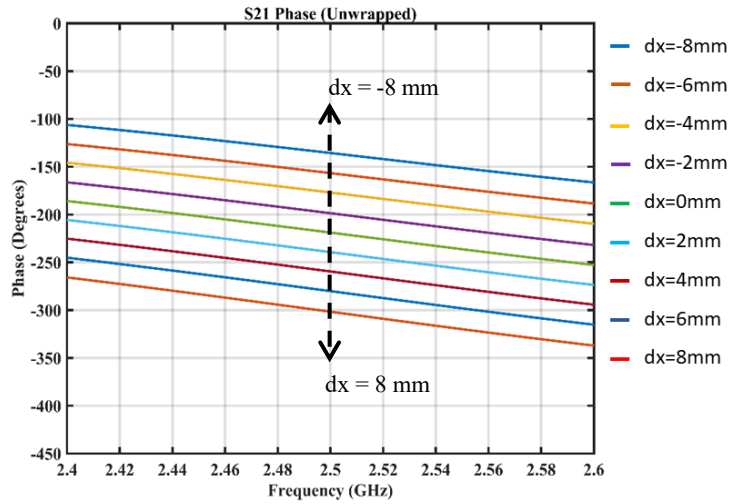

(b)

Figure 4-22 Simulated phase of the a) Reflection coefficient, b) Transmission coefficient for different values of displacement dx from −8 to 8 mm in steps of 2 mm.

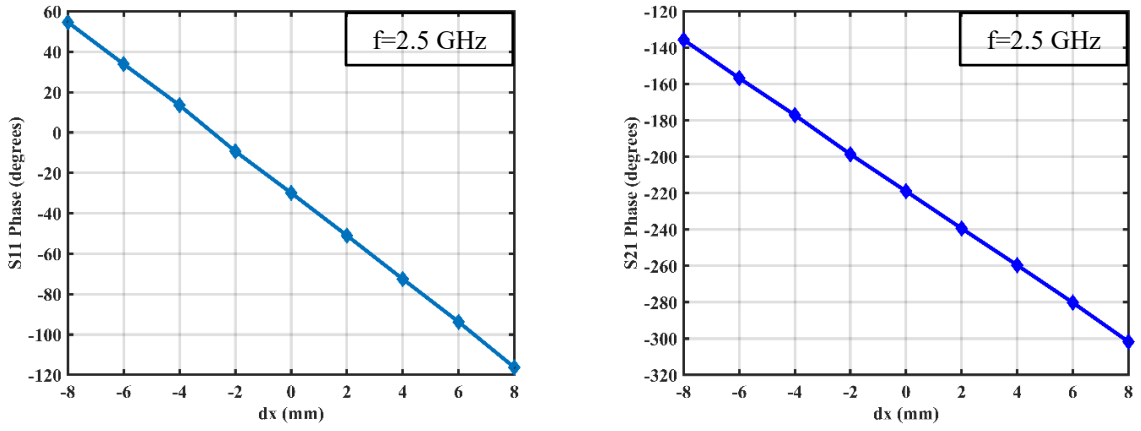

(a) (b)

Figure 4-23 Simulated phase of the reflection and transmission coefficient in terms of displacement dx at the resonance frequency of the pair of SRRs f = 2.5 GHz.

4.4.2 Michelson Interferometric Configuration Analysis

Figure 4-24 illustrates the simulated proposed Michelson sensor using Via as a shorted to ground between the two output ports of a branch-line coupler to convert phase information to magnitude information on full-wave simulation CST.

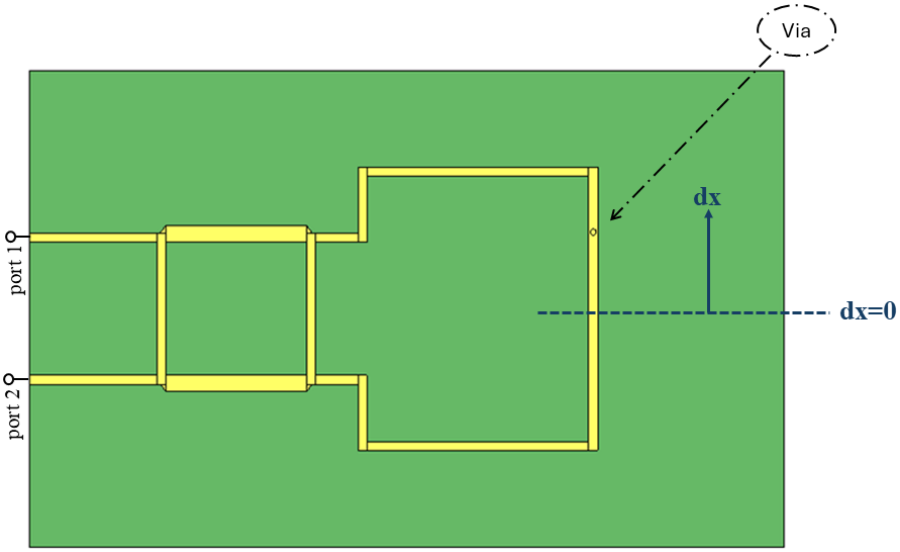

Figure 4-24 Configuration of a branch-line coupler to convert phase information to magnitude information for different values of displacement.

Simulated transmission coefficient (S(2,1)) of the structure proposed in 4-24 is illustrated in Figure 4-25. Further analysis reveals that transmission coefficient decreases as following at the resonance frequency.

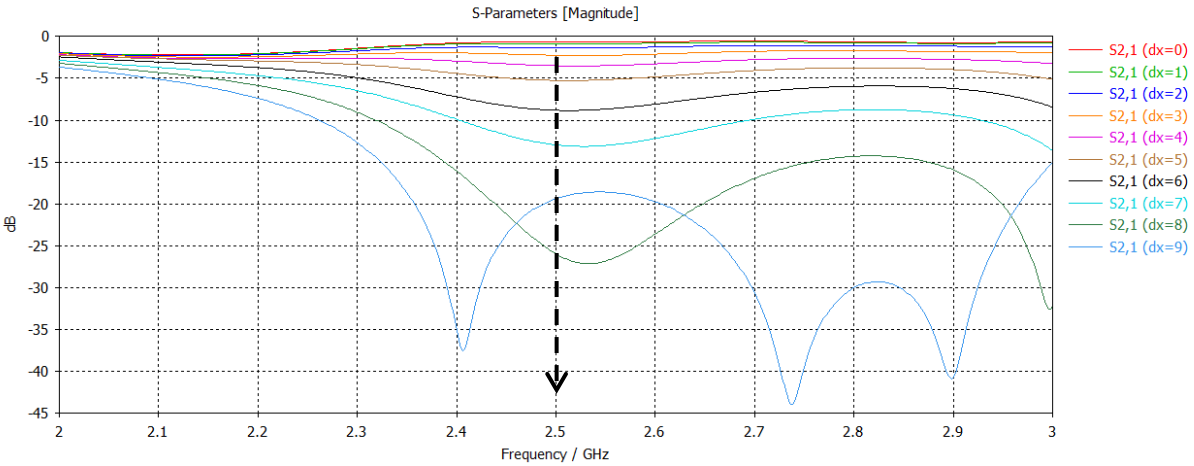

Figure 4-25 Simulated transmission coefficient (S(2,1)) for different values of displacement.

4.4.3 Michelson Interferometric Final Design

Figure 4-26 illustrates the simulated proposed Michelson sensor between the two output ports of a branch-line coupler to convert phase information to magnitude information on full-wave simulation CST.

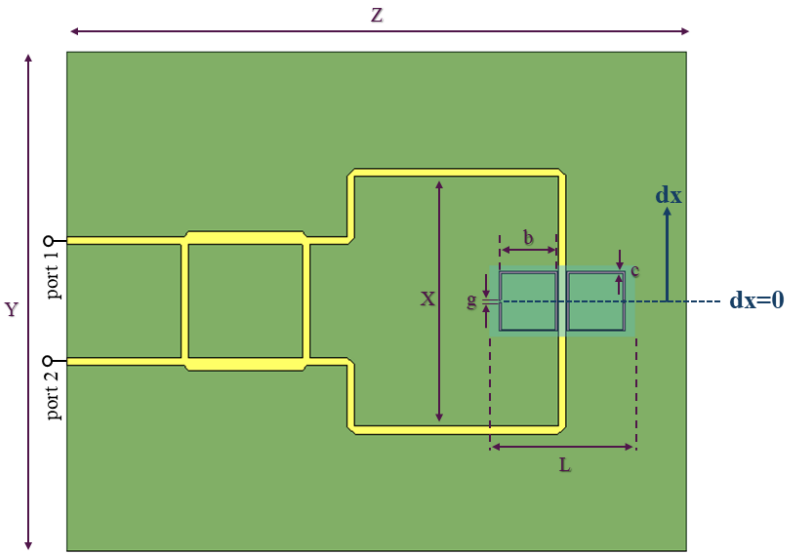

Parameter	Dimensions(mm)
b	8.9
c	0.3
g	0.3
L	21.6
X	37
Y	72
Z	91.4

Figure 4-26 Simulated proposed Michelson sensor.

Figure 4-27 presents the simulated reflection and transmission coefficients for different displacement values (dx) at the operating frequency of 2.5 GHz, obtained by using the CST full-wave simulator.

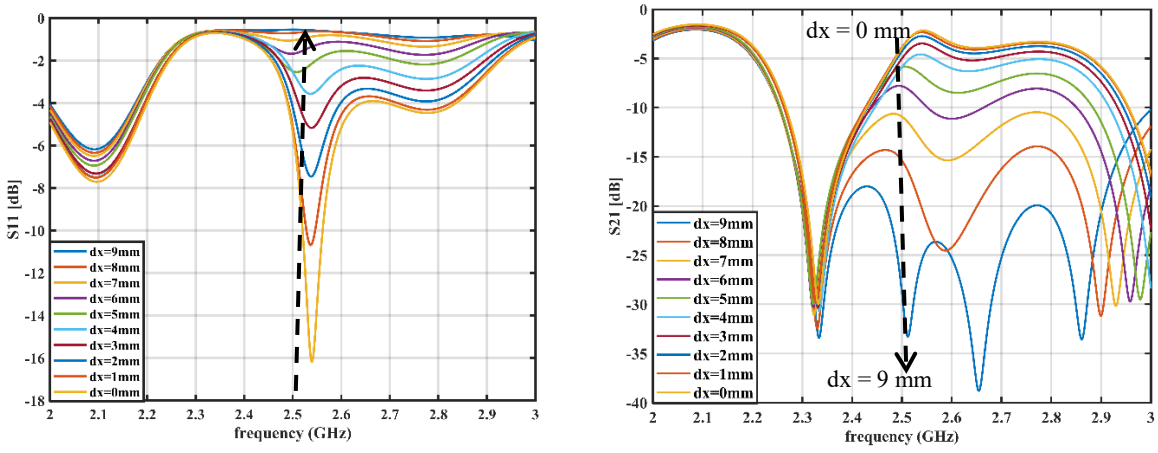

(a) (b)

Figure 4-27 Simulated magnitude of a) reflection and b) transmission coefficients of the proposed sensor versus frequency for different values of displacement dx.

This HFSS simulation in Figure 4-28, shows a microwave Michelson interferometric sensor with detailed mesh highlighting its path and surface, using a coarse mesh

on the microstrip line and SRR gap while keeping the rest of the substrate sparsely meshed.

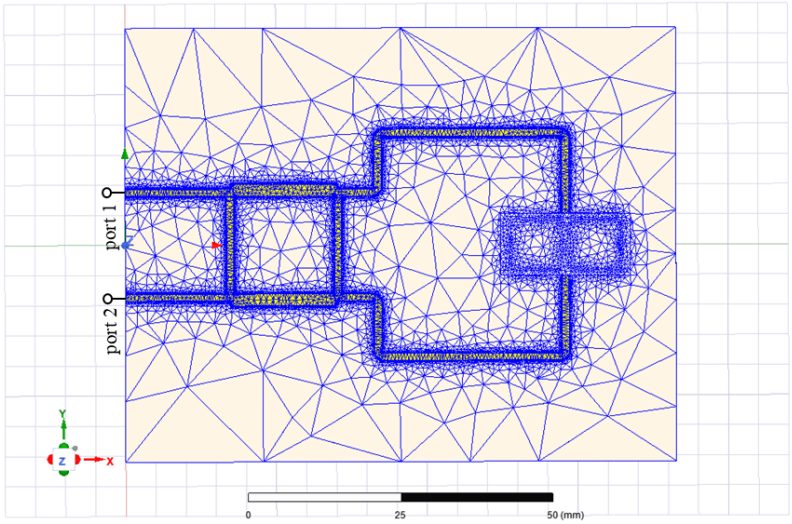

Figure 4-28 HFSS Mesh View of proposed Mickelson Sensor.

Figure 4-29 illustrates the simulation results for reflection and transmission coefficients for different values of displacement dx at the operating frequency of 2.5 GHz, resulted from HFSS full-wave simulator.

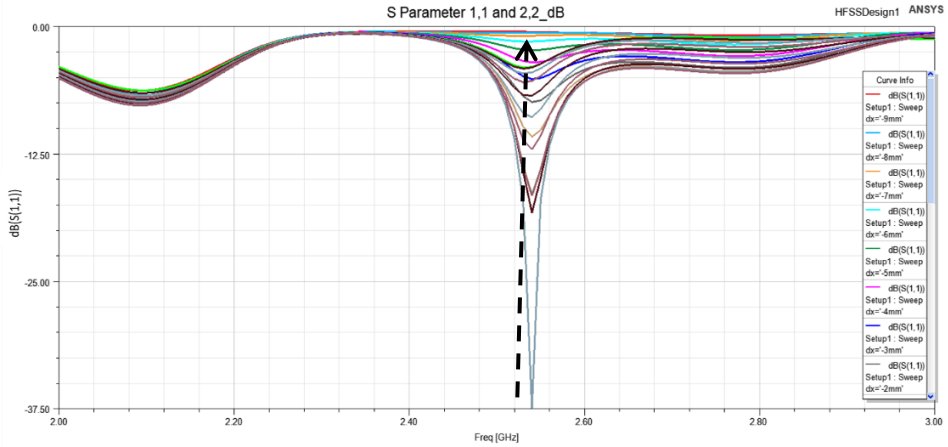

(a)

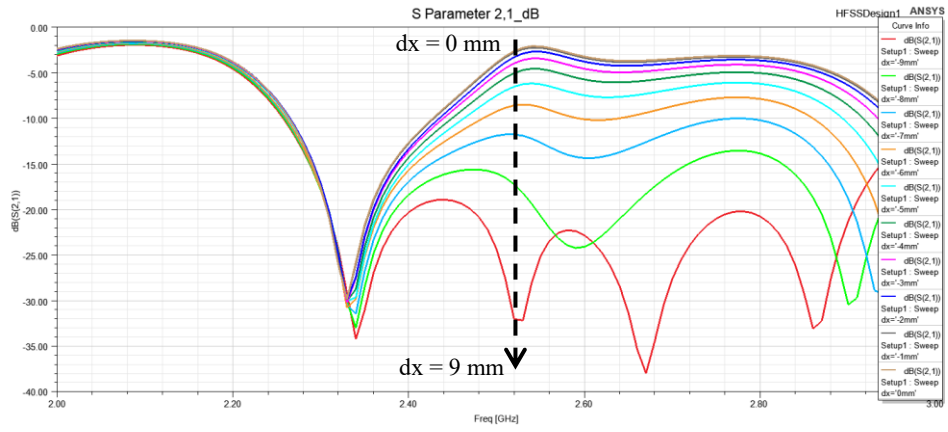

(b)

Figure 4-29 Simulated amplitude of a) Reflection, b) Transmission coefficient for different values of displacement dx.

At the glance of Figure 4-30, the normalized simulated transmission coefficients versus dx of the proposed Mickelson sensor at the resonance frequency between adjacent ports. Further evaluation of this figure reveals that the slope of this figure shows an average sensitivity of approximately 2.6dB/mm, which can be known as proper sensitivity leading in accurate location detection.

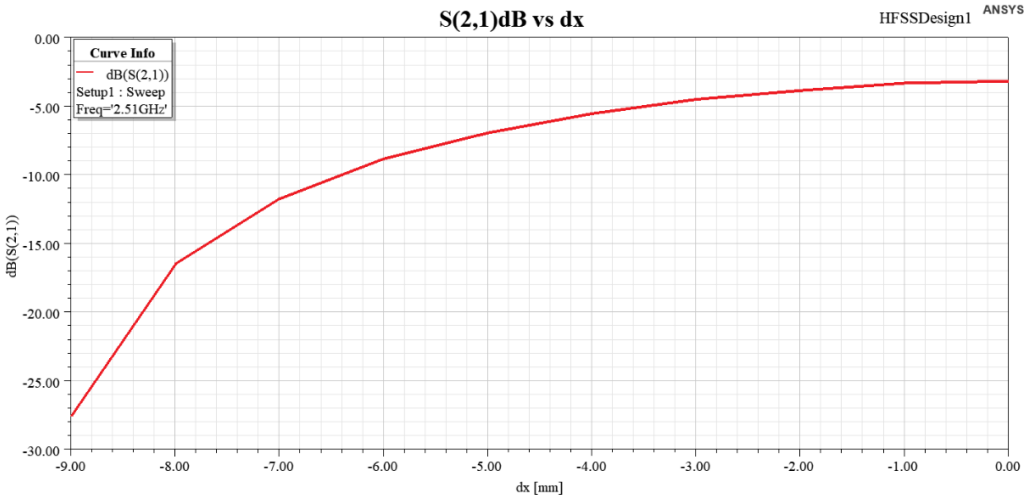

Figure 4-30 Normalized simulated transmission coefficients versus dx of the proposed Mickelson sensor at the resonance frequency.

The experimental analysis of the Michelson interferometric displacement sensor including Fabricated prototype and Measurement setup are demonstrated in Figure 4-31. The scattering parameters are measured utilizing an Agilent PNA-X N5242A, a high-performance vector network analyzer (VNA).

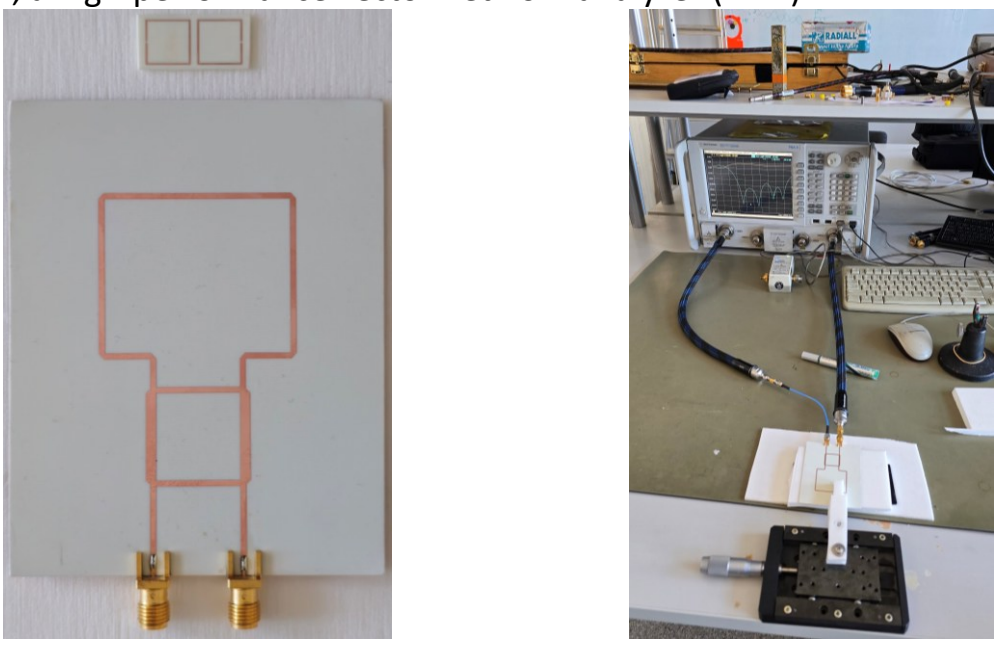

(a) (b)

Figure 4-31 Experimental Analysis of Michelson interferometric displacement sensor. a) Fabricated prototype, b) Measurement setup.

Figure 4-32 illustrates the results of measured scattering parameters of the structure shown in Figure 4-31. The S-Parameters are measured with the 3mm steps of displacement. Despite the inaccuracy in fabrication and measurement process, which appears as 240MHz frequency shift, the experimental and simulation analysis allies with each other.

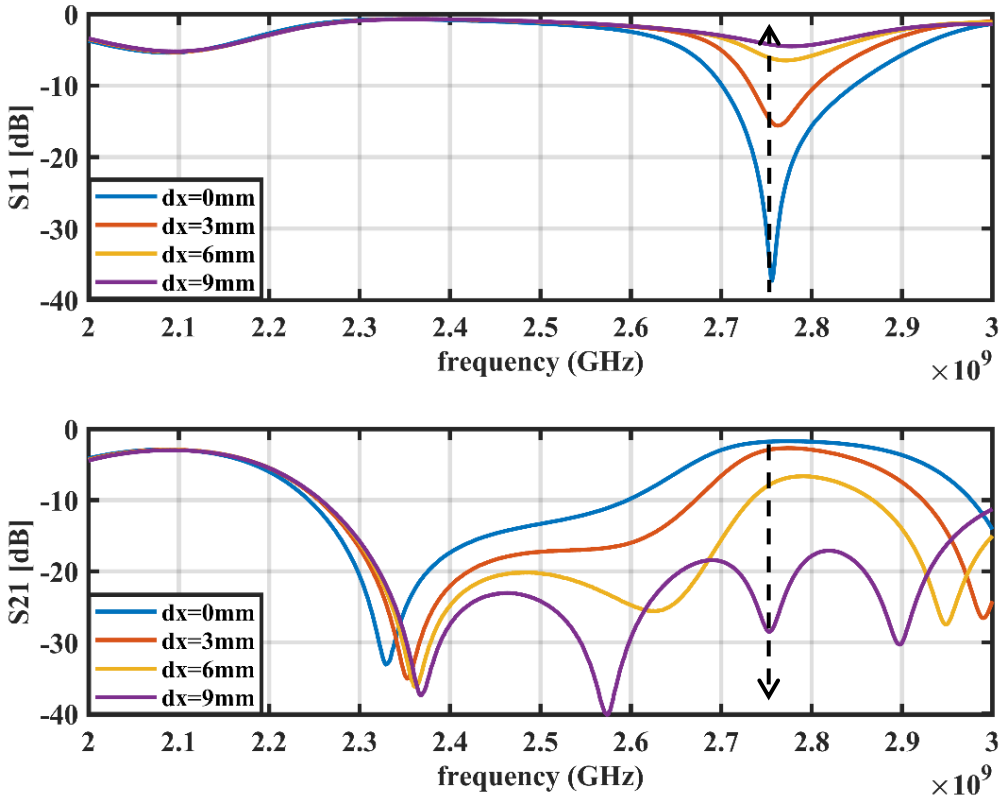

Figure 4-32 Measured results of proposed Michelson Interferometric displacement sensor.

4.4.4 Mach Zehnder Interferometric Design

Figure 4-33 illustrates the simulated proposed Mach Zehnder interferometric sensor between four output ports of both branch-line coupler and normalized four other ports with 50ohm resistors to convert phase information to magnitude information on full-wave simulation CST with dimensions.

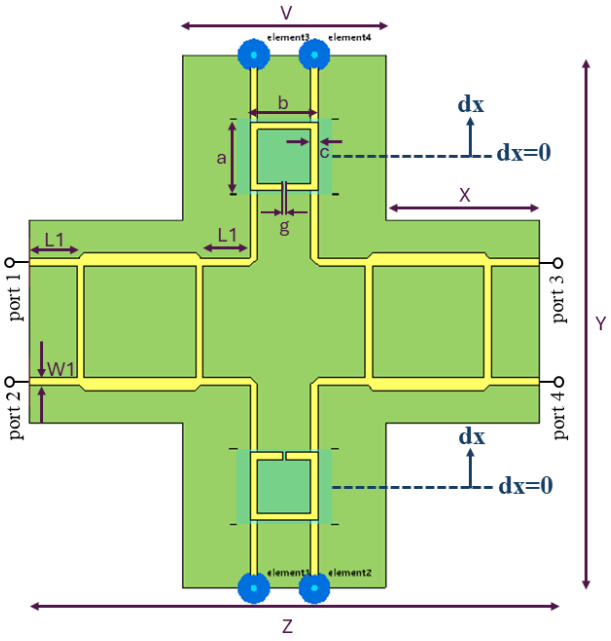

Parameter	Dimensions(mm)
W1	1.1
L1	7
a	11
b	8.5
c	1
g	0.5
V	30
X	22.8
Y	78.8
Z	75.5

Figure 4-33 Geometry of proposed Mach-Zehnder interferometric sensor.

Figure 4-34 Simulated amplitude of Reflection and Transmission coefficients for different values of displacement dx at the operating frequency of 2.5GHz, resulted from CST full-wave simulator.

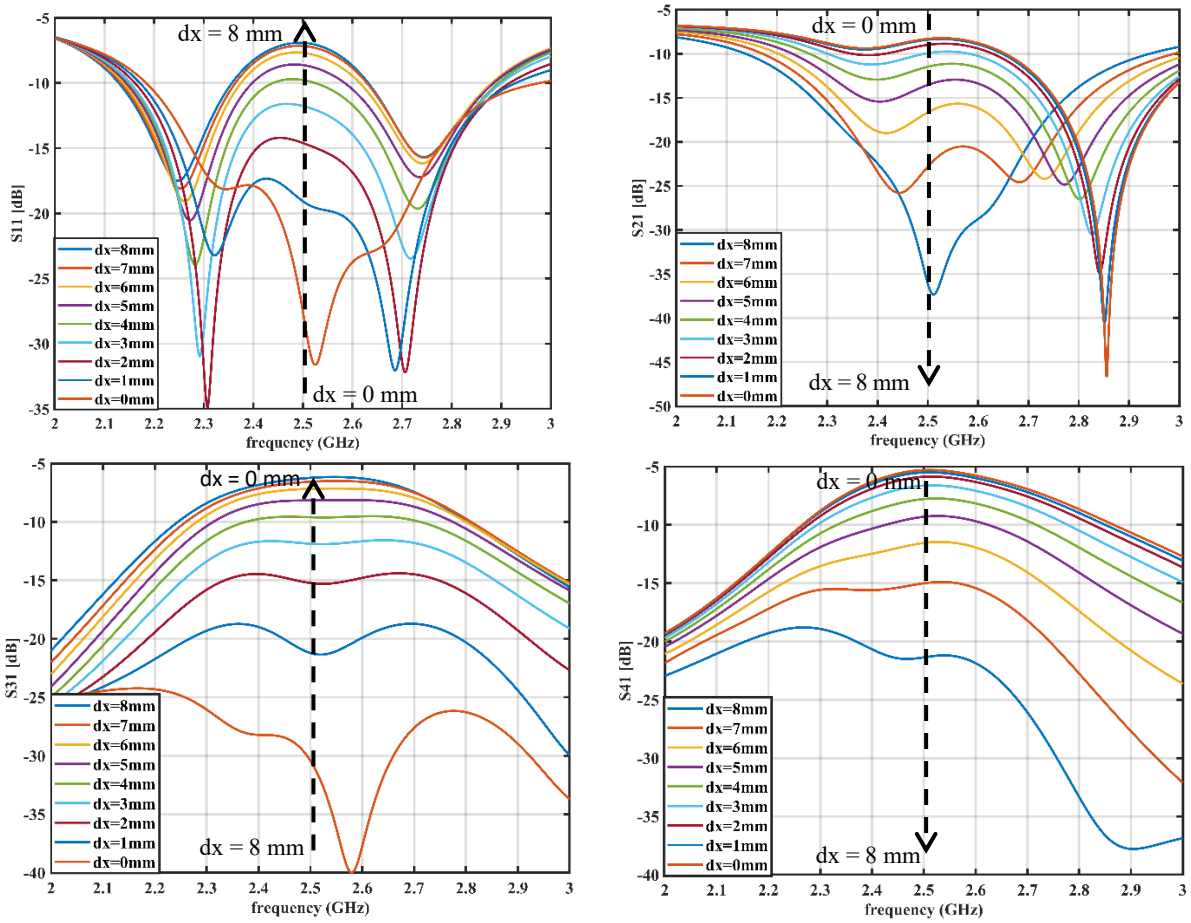

Figure 4-34 Simulated S-Parameters of Mach-Zehnder sensor.

At the glance of Figure 4-35, the normalized simulated transmission coefficients versus dx of the proposed Mach-Zehnder sensor at the resonance frequency by considering reciprocity between adjacent ports. Further evaluation of this figure reveals that the slope of transmission coefficient shows an average sensitivity of approximately 3.6dB/mm, which can be known as proper sensitivity leading in accurate location detection.

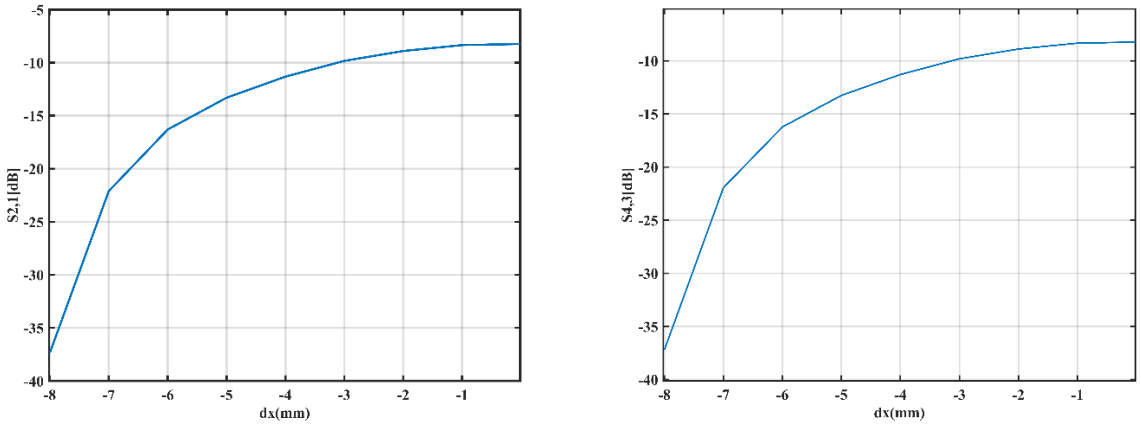

Figure 4-35 Normalized simulated transmission coefficients versus dx of the proposed Mach-Zehnder sensor at the resonance frequency.

Evaluating Figure 4-36, it can be observed that while the SRR probe is placed in dx=0, the excited power from port 1 is divided between ports 2 and 4 respectively; However, for position of dx=8, most of the excited power flows to port 3.
This characteristic can be utilized to sense the position of SRR probe, which is the main functionality of the Mach-Zehnder interferometric displacement sensor.

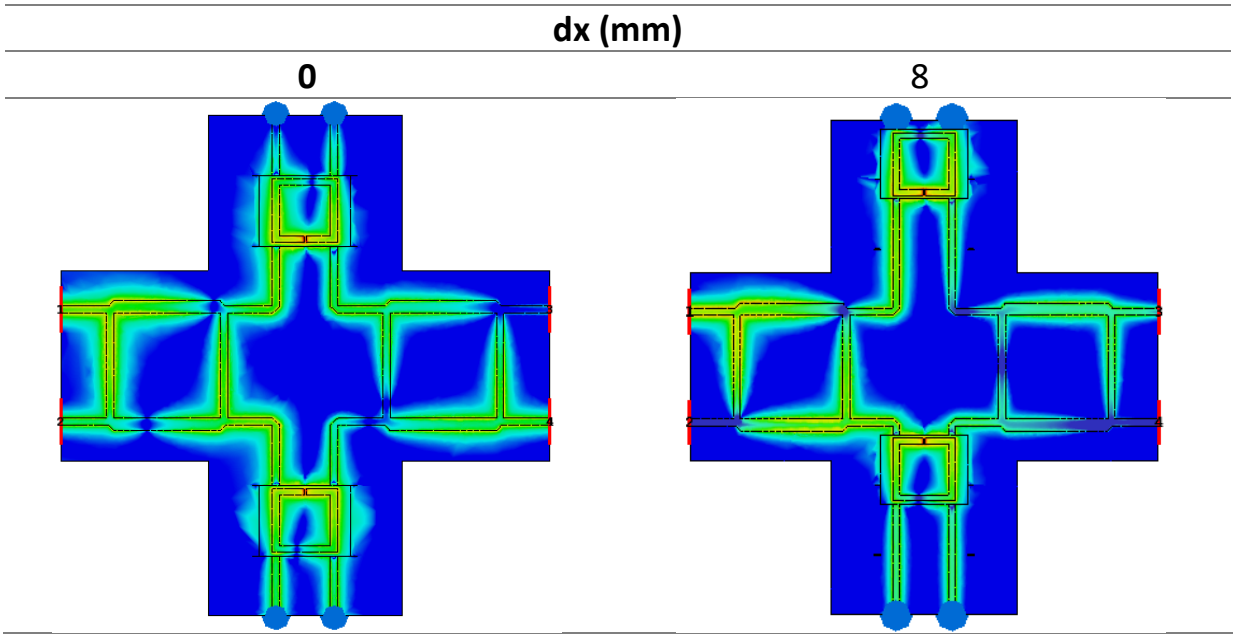

Figure 4-36 Power flow between inputs & outputs of Mach-Zehnder.

The experimental analysis of the Mach Zehnder Interferometric displacement sensor including Fabricated prototype and Measurement setup are illustrated in Figure 4-37. The scattering parameters are measured utilizing an Agilent PNA-X N5242A VNA.

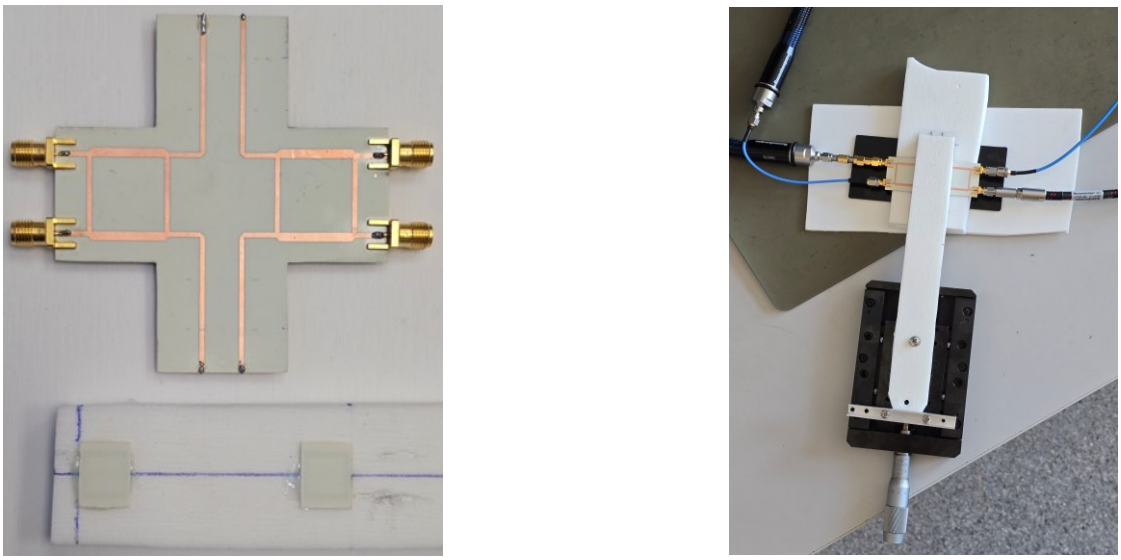

(a) (b)

Figure 4-37 Experimental Analysis of Mach Zehnder Interferometric displacement sensor. a) Fabricated prototype, b) Measurement setup.

Figure 4-38 illustrates the results of measured scattering parameters of the structure shown in Figure 4-37.

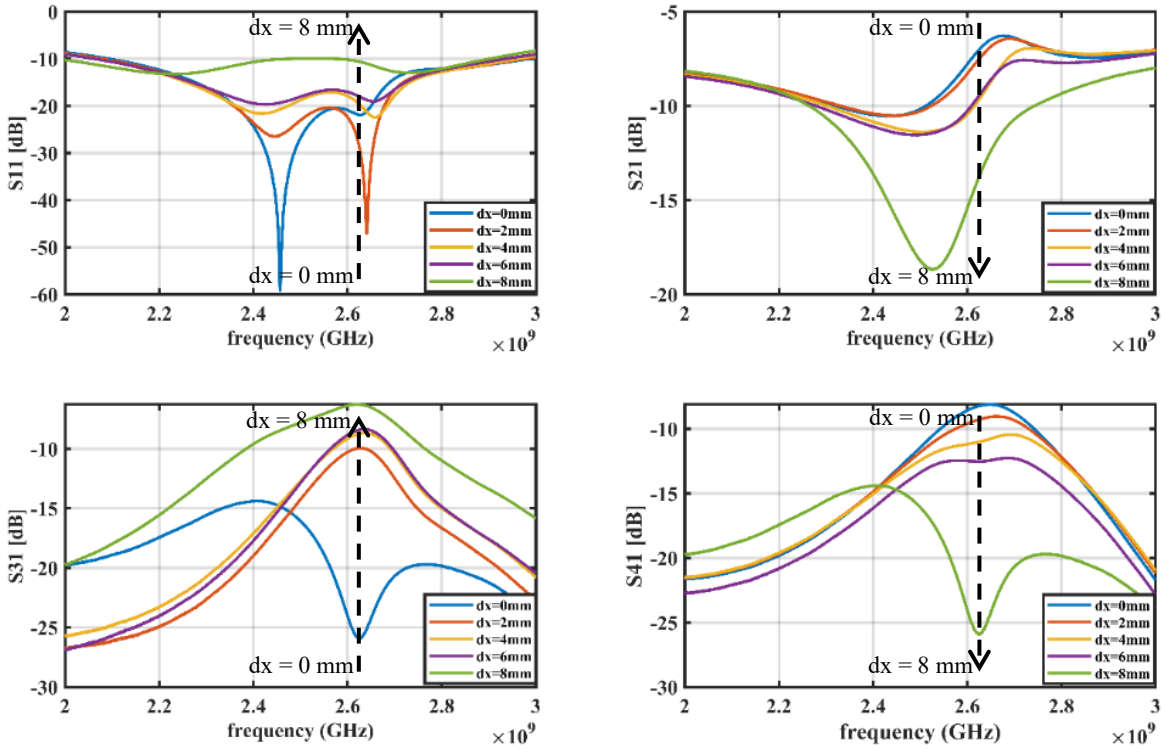

Figure 4-38 Measured results of proposed Mach Zehnder Interferometric displacement sensor.

The S-Parameters are measured with the 2mm steps of displacement. Despite the inaccuracy in fabrication and measurement process, which appears as 240MHz frequency shift, the experimental and simulation analysis allies with each other. Figure 4-39 presents the normalized experimental analysis of the fabricated Mach-Zehnder prototype, without SRR probe.

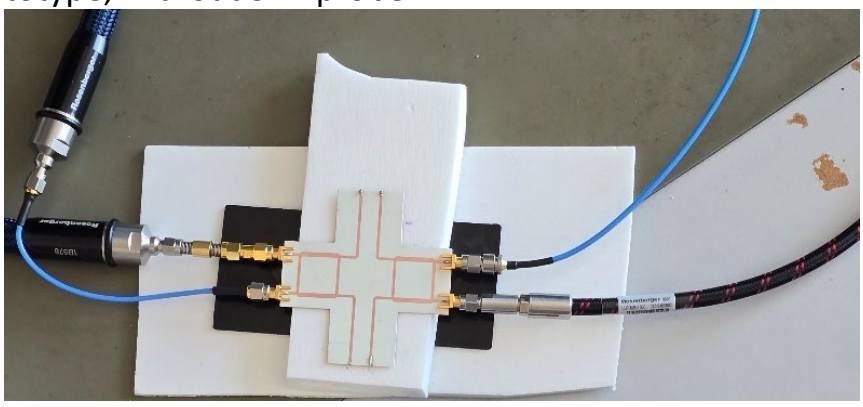

Figure 4-39 Experimental Analysis of the fabricated Mach Zehnder prototype.

As shown in Figure 4-40, the simulated and measured results of the fabricated Mach Zehnder denoted perfect matching in the specified resonance frequency.

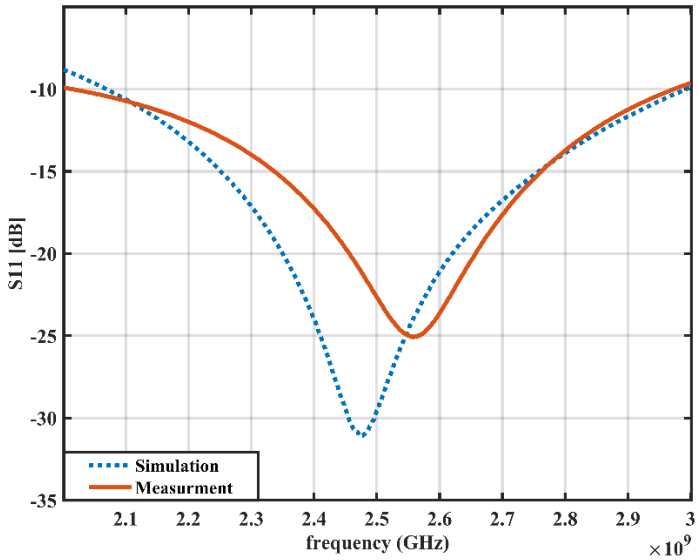

Figure 4-40 Simulated and Measure results of fabricated Mach Zehnder.

Table 4-3 summarizes a detailed comparison between Michelson and Mach-Zehnder Interferometric displacement sensors, evaluating sensitivity, dimensions and numbers of SRR probes.

Table 4-3 Comparison between two different mentioned displacement sensors.

	Sensitivity	Dimensions	NO.SRR probes
Michelson	2.6 (dB/mm)	91.4 x 72 (mm^2)	1
Mach Zehnder	3.6 (dB/mm)	78.8 x 75.5 (mm^2)	2

Chapter 5:

Conclusion and Future Work

Conclusion:

This thesis successfully demonstrates the design and development of a microwave displacement sensor that operates by analyzing phase variations. Key components of the sensor such as microstrip lines, SRRs, and interferometric configurations were thoroughly examined through theoretical modeling, simulations, and practical experiments. Some important achievements are mentioned below:

High Sensitivity and Linearity: The sensor offers high sensitivity along with a clear, linear response, making it well-suited for precise displacement measurements. In the Mach-Zehnder setup, it reached a sensitivity of 3.6 dB/mm with a steady phase response. In the Michelson interferometer setup, it showed a sensitivity of 2.6 dB/mm. These results demonstrate the sensor's accuracy and reliability.

Interferometric Advantages: The sensor simplified measurement complexity by converting phase shifts into amplitude variations, while maintaining accuracy.

Versatility: The design can easily be accommodated for other purposes such as humidity measurement or material analysis, just by adjusting the shape of the resonators.

Experimental Validation: Fabricated prototypes confirmed that the design works as expected, with test results matching simulations closely.

Future Work:

- Miniaturization for integration into compact systems.
- Exploration of multi-axis displacement sensing.
- Enhanced wireless connectivity to let the sensor send data in real time.
- Application particular Improvements, such as biomedical monitoring or industrial robotics.

In summary, this work advances microwave sensing technology by offering a robust, high-precision solution for displacement measurement, with broad potential for future innovations in sensing and automation.

Bibliography

[1] X. Wang, J. G. Liang, J. K. Wu, X. F. Gu, and N. Y. Kim, “Microwave Detection with Various Sensitive Materials for Humidity Sensing,” *Sens Actuators B Chem*, vol. 351, 2022.

[2] J. Yeo and Y. Kwon, “Gelatin-Coated High-Sensitivity Microwave Sensor for Humidity-Sensing Applications,” *Sensors*, vol. 24, no. 19, 2024.

[3] J. K. Park, T. G. Kang, B. H. Kim, H. J. Lee, H. H. Choi, and J. G. Yook, “Real-Time Humidity Sensor Based on Microwave Resonator Coupled with PEDOT: PSS Conducting Polymer Film,” *Sci Rep*, vol. 8, no. 1, 2018.

[4] L. Su, P. Vélez, P. Casacuberta, J. Muñoz-Enano, and F. Martín, “Microwave Humidity Sensor for Early Detection of Sweat and Urine Leakage,” *Electronics*, vol. 12, no. 10, 2023.

[5] L. C. Fan, W. S. Zhao, D. W. Wang, Q. Liu, S. Chen, and G. Wang, “An Ultrahigh Sensitivity Microwave Sensor for Microfluidic Applications,” *IEEE Microwave and Wireless Components Letters*, vol. 30, no. 12, pp. 1201–1204, 2020.

[6] C. Ds, K. B. S. S. Nagini, R. K. Barik, and S. Koziel, “Highly Sensitive Microwave Sensors Based on Open Complementary Square Split-Ring Resonator for Sensing Liquid Materials,” *Sensors*, vol. 24, no. 6, 2024.

[7] X. Han, X. Li, Y. Zhou, Z. Ma, P. Peng, C. Fu and L. Qiao “Microwave Sensor Loaded with Complementary Curved Ring Resonator for Material Permittivity Detection,” *IEEE Sens J*, vol. 22, no. 21, pp. 20456–20463, 2022.

[8] Z. Shaterian, A. K. Horestani, F. Martín, and M. Mrozowski, “Design of Novel Highly Sensitive Sensors for Crack Detection in Metal Surfaces: Theoretical Foundation and Experimental Validation,” *Sci Rep*, vol. 13, no. 1, 2023.

[9] B. Qian, L. Mou, L. Wu, Z. Xiao, T. Hu, and J. Jiang, “A Direction-Sensitive Microwave Sensor for Metal Crack Detection,” *Applied Sciences (Switzerland)*, vol. 12, no. 18, 2022.

[10] Z. Shaterian and M. Mrozowski, "Crack Detection in Metallic Surfaces Based on Dumbbell-Shaped Defected Ground Structures in Microstrip Technology." *In 2022 24th International Microwave and Radar Conference (MIKON)*, pp. 1-4. IEEE, 2022.

[11] A. M. Albishi and O. M. Ramahi, “Microwaves-Based High Sensitivity Sensors for Crack Detection in Metallic Materials,” *IEEE Trans Microwave Theory Tech*, vol. 65, no. 5, pp. 1864–1872, 2017.

[12] H. Kou, Q. Tan, Y. Wang, G. Zhang, S. Shujing, and J. Xiong, “A Microwave SIW Sensor Loaded with CSRR for Wireless Pressure Detection in High-Temperature Environments,” *J Phys D Appl Phys*, vol. 53, no. 8, 2020.

[13] Z. Mehrjoo, A. Ebrahimi, and K. Ghorbani, “Microwave Resonance-Based Reflective Mode Displacement Sensor with Wide Dynamic Range,” *IEEE Trans Instrum Meas*, vol. 71, 2022.

[14] C. H. Chio, K. W. Tam, and R. Gomez-Garcia, “Filtering Angular Displacement Sensor Based on Transversal Section with Parallel-Coupled-Line Path and U-Shaped Coupled Slotline,” *IEEE Sens J*, vol. 22, no. 2, pp. 1218–1226, 2022.

[15] Z. Zhang, C. H. Chio, K. W. Tam, G. Zhang, X. Zhou, C. Teng, N. Kong., “Microwave Displacement Sensors Based on Filtering Phase Shifter with Chebyshev Response,” *IEEE Sens J*, vol. 24, no. 10, pp. 15857–15864, 2024.

[16] A. K. Horestani, C. Fumeaux, S. F. Al-Sarawi, and D. Abbott, “Displacement Sensor Based on Diamond-Shaped Tapered Split Ring Resonator,” *IEEE Sens J*, vol. 13, no. 4, pp. 1153–1160, 2013.

[17] Z. Shaterian and M. Mrozowski, “Multifunctional Bandpass Filter/Displacement Sensor Component,” *IEEE Access*, vol. 11, pp. 27012-27019, 2023.

[18] A. K. Jha, N. Delmonte, A. Lamecki, M. Mrozowski, and M. Bozzi, “Design of Microwave-Based Angular Displacement Sensor,” *IEEE Microwave and Wireless Components Letters*, vol. 29, no. 4, pp. 306–308, 2019.

[19] T. Reininger, F. Welker, and M. V. Zeppelin, “Sensors in Position Control Applications for Industrial Automation,” *Sens Actuators A: Physical*, vol. 129, no. 1-2, pp. 270–274, 2006.

[20] B. Camli, E. Kusakci, B. Lafci, S. Salman, H. Torun, and A. Yalcinkaya, “A Microwave Ring Resonator Based Glucose Sensor,” in *Procedia Engineering*, Elsevier Ltd, pp. 465–468, 2016.

[21] R. Patel and N. Correll, “Integrated Force and Distance Sensing Using Elastomer-Embedded Commodity Proximity Sensors.” *Robotics: Science and Systems*, 2016.

[22] A. N. Moqadam and R. Kazemi, “High-Resolution Imaging of Narrow Bone Fractures with a Novel Microwave Transceiver Sensor Utilizing Dual-Polarized RIS and SRR Array Antennas,” *IEEE Sens J*, vol. 23, no. 24, pp. 30335–30344, 2023.

[23] X. Liu, K. Peng, Z. Chen, H. Pu, and Z. Yu, “A New Capacitive Displacement Sensor with Nanometer Accuracy and Long Range,” *IEEE Sens J*, vol. 16, no. 8, pp. 2306–2316, 2016.

[24] A. H. Arroyo, G. Overton, A. J. Mulholland, and R. R. Hughes, “Displacement Sensing Using Bi-Modal Resonance in Over-Coupled Inductors,” *Sensors*, vol. 25, no. 6, 2025.

[25] Z. Zhang, Z. Zhang, D. Mei, and Y. Wang, “Multifunctional Flexible Sensor with Both Contact Pressure Sensing and Internal Ultrasonic Detection for Robotic Grasping,” *Sens Actuators A: Physical*, vol. 383, 2025.

[26] C. C. Hsu, H. Chen, H. Y. Tseng, S. C. Lan, and J. Lin, “High Displacement Resolution Encoder by Using Triple Grating Combination Interferometer,” *Opt Laser Technol*, vol. 105, pp. 221–228, 2018.

[27] J. Polivka, “An Overview of Microwave Sensor Technology,” *High Frequency Electronics*, vol. 6, no. 4, pp. 32-42, 2007.

[28] M. A. Belen, P. Mahouti, F. Güneş, and H. P. Partal, “Design and Implementation of Doppler Microwave Motion Sensor for Indoor Application,” *Sigma Journal of Engineering and Natural Sciences,* vol. 36, no. 3, pp. 849-859. 2018.

[29] E. Guerrero, J. Brugues, J. Verdu, and P. De Paco, “Microwave Microphone Using a General Purpose 24-GHz FMCW Radar,” *IEEE Sens Lett*, vol. 4, no. 6, 2020.

[30] A. K. Horestani, “Microwave Displacement Sensor with Good Linearity and Dynamic Range Based on a Microstrip Line Pair Loaded with Movable Electric-LC Resonators,” *IEEE Sens J*, no. 62, pp. 1–10, 2024.

[31] A. K. Horestani and F. Paredes, “Phase-Variation Microwave Displacement Sensor with Good Linearity and Application to Breath Rate Monitoring,” *IEEE Sens J*, vol. 23, no. 62, pp. 1–10, 2023.

[32] Z. Shaterian and M. Mrozowski, “Displacement Sensors Based on the Phase of the Reflection Coefficient of a Split Ring Resonator-Loaded Transmission Line,” *IEEE Sens J*, vol. 22, no. 21, pp. 20321–20327, 2022.

[33] A. K. Horestani, Z. Shaterian, and M. Mrozowski, “A Compact and Lightweight Microwave Tilt Sensor Based on an SRR-Loaded Microstrip Line,” in *2022 24th International Microwave and Radar Conference, MIKON 2022*, Institute of Electrical and Electronics Engineers Inc., 2022.

[34] D. M. Pozar, "Microwave Engineering." Fourth Editions, John Wiley & Sons, (2012).

[35] N. Alrayes and M. I. Hussein, “Metamaterial-Based Sensor Design Using Split Ring Resonator and Hilbert Fractal for Biomedical Application,” *Sens Biosensing Res*, vol. 31, 2021.

Appendix

A. The MATLAB code of gamma derivation for BLHC with dual grounded ports:

```
close all;
clear ;

A = 1;
magnitude = 0.5;
k = (A / 2) * magnitude;
fprintf('k: %.2f\n', k);
ph2 = -180 : 1 : 180;
ph3 = -180 : 1 : 180;

[PH2, PH3] = meshgrid(ph2, ph3);

f1 = ((exp(-1i * deg2rad(PH3))) - (exp(-1i * deg2rad(PH2))))*k ;
f2 = ((exp(-1i * deg2rad(PH3))) + (exp(-1i * deg2rad(PH2))))*k ;

abs_f1 = abs(f1);
abs_f2 = abs(f2);

subplot(2,1,1);
surf(ph2, ph3, abs_f1);
xlabel('ph2 (degrees)');
ylabel('ph3 (degrees)');
zlabel('|f1|');
title('Surface Plot of |f1|');
colormap jet;
colorbar;
shading interp;

subplot(2,1,2);
surf(ph2, ph3, abs_f2);
xlabel('ph2 (degrees)');
ylabel('ph3 (degrees)');
zlabel('|f2|');
title('Surface Plot of |f2|');
colormap jet;
colorbar;
shading interp;
figure;
plot(ph3,abs_f1(1,:),ph3,abs_f2(1,:));
```

B. The MATLAB code for analysis of reflection coefficient of a BLHC with two grounded ports vs one variable length:

```
close all;
clear ;

f = 2.5e9;
c = 2e8;
B = 2 * 3.1415 * f / c;
L3 = 0.5e-3 : 0.1e-3 : 35.5e-3;

Gamma_L3_values = zeros(1, length(L3));

for idx = 1:length(L3)
   Gamma_L3_values(idx) = (1i * tan(B * L3(idx)) - 1) ./ (1i * tan(B * L3(idx)) + 1);
end

grid on;
L2 = 17e-3*ones(1, length(L3));
Gamma_L2_values = ((1i * tan(B * L2) - 1) ./ (1i * tan(B * L2) + 1));

S_11 = 0.5 * (Gamma_L2_values - Gamma_L3_values);
S_41 = 0.5 * i * (Gamma_L2_values + Gamma_L3_values);

subplot(2,2,1);
plot(L3*1000 , 10 * log10 (abs(S_11)));
xlabel('L3 (mm)');
ylabel('S11 (dB)');
subplot(2,2,2);
plot(L3*1000 , angle(S_11)*180/pi);
xlabel('L3 (mm)');
ylabel('Phase S11 (degree)');
subplot(2,2,3);
plot(L3*1000 , 10 * log10 (abs(S_41)));
xlabel('L3 (mm)');
ylabel('S41 (dB)');
subplot(2,2,4);
plot(L3*1000 , angle(S_41)*180/pi);
xlabel('L3 (mm)');
ylabel('Phase S41 (degree)');
figure;
hold on
plot(L3*1000 , 20 * log10 (abs(S_11)));
plot(L3*1000 , 20 * log10 (abs(S_41)));
xlabel('L_2 (mm)');
ylabel('S11  &  S21 (dB)');
hold off
```